

EFFECTS OF MAGNETIC AND KINETIC HELICITIES ON THE GROWTH OF MAGNETIC FIELDS IN LAMINAR AND TURBULENT FLOWS BY HELICAL-FOURIER DECOMPOSITION

MORITZ LINKMANN^{1,2}, GANAPATI SAHOO¹, MAIRI MCKAY², ARJUN BERERA², LUCA BIFERALE¹

¹Department of Physics & INFN, University of Rome Tor Vergata, Via della Ricerca Scientifica 1, 00133 Rome, Italy.

²School of Physics and Astronomy, University of Edinburgh, Peter Guthrie Tait Road, EH9 3FD, Edinburgh, UK.

(Dated: May 16, 2022)

ABSTRACT

We present a numerical and analytical study of incompressible homogeneous conducting fluids using a Fourier-helical representation. We analytically study both small- and large-scale dynamo properties, as well as the inverse cascade of magnetic helicity, in the most general minimal subset of interacting velocity and magnetic fields on a closed Fourier triad. We mainly focus on the dependency of magnetic field growth as a function of the distribution of kinetic and magnetic helicities among the three interacting wavenumbers. By combining direct numerical simulations of the full magnetohydrodynamics (MHD) equations with the Fourier-helical decomposition we numerically confirm that in the kinematic dynamo regime the system develops a large-scale magnetic helicity with opposite sign compared to the small-scale kinetic helicity, a sort of triad-by-triad α -effect in Fourier space. Concerning the small-scale perturbations, we predict theoretically and confirm numerically that the largest instability is achieved for the magnetic component with the same helicity of the flow, in agreement with the Stretch-Twist-Fold mechanism. Viceversa, in presence of a Lorentz feedback on the velocity, we find that the inverse cascade of magnetic helicity is mostly local if magnetic and kinetic helicities have opposite sign, while it is more non-local and more intense if they have the same sign, as predicted by the analytical approach.

Our analytical and numerical results further demonstrate the potential of the helical-Fourier decomposition to elucidate the entangled dynamics of magnetic and kinetic helicities both in fully developed turbulence and in laminar flows.

1. INTRODUCTION

Turbulent flows are ubiquitous on the earth and in the sky, e.g. (Frisch 1995; Pope 2000). In many astrophysical and geophysical cases (Belenkaya 2009), the fluid is also conducting and one needs to control the entangled dynamics of velocity and magnetic fields, this is the case of MHD turbulence (Moffatt 1978; Biskamp 2003; Verma 2004). The spectrum of possible configurations and applications is vast, depending on the presence of particular external forcing mechanisms, mean flows/fields and boundaries (Priest & Forbes 2000; Priest 2014; Plihon et al. 2014; Stieglitz & Müller 2001; Gailitis et al. 2000, 2001; Goodman & Ji 2002; Nornberg et al. 2006; Frick et al. 2010). Here we want to address basic properties of all MHD configurations connected with the interactions leading to the transfer of total energy, magnetic helicity and kinetic helicity across scales. For MHD, the presence of three inviscid invariants, total energy, magnetic and cross-helicity, makes the problem of predicting spectral properties difficult (Iroshnikov 1964; Kraichnan 1965; Matthaeus & Zhou 1989; Goldreich & Sridhar 1995; Boldyrev 2005a,b). Even the direction of the different transfers is not completely under control, only empirical results exist (Biskamp 2003). Moreover, because of obvious applied and fundamental issues, predicting/controlling the growth rate of a magnetic field is a key question, connected to the famous dynamo problem (Moffatt 1969; Krause & Rädler 1980; Brandenburg 2003; Brandenburg & Subramanian 2005; Tobias et al. 2013). Since the magnetic energy is not conserved, the magnetic field may stretched/folded/advected even in absence of external input and dissipation. A huge amount of literature has been devoted to the identification of the key dynamical and statistical ingredients needed to promote or deplete such a growth and to control the growth

rate. Magnetic and kinetic helicities are among the key quantities that play a role in such a phenomenon:

$$H_m(t) = \int_V d\mathbf{x} \mathbf{a}(\mathbf{x}, t) \cdot \mathbf{b}(\mathbf{x}, t) , \quad (1)$$

$$H_k(t) = \int_V d\mathbf{x} \mathbf{u}(\mathbf{x}, t) \cdot \boldsymbol{\omega}(\mathbf{x}, t) , \quad (2)$$

$$(3)$$

where \mathbf{u} , \mathbf{b} , \mathbf{a} and $\boldsymbol{\omega}$ are the velocity, the magnetic field, the magnetic vector potential and the vorticity, respectively. The third ideal invariant of the MHD equations is given by cross-helicity:

$$H_c(t) = \int_V d\mathbf{x} \mathbf{u}(\mathbf{x}, t) \cdot \mathbf{b}(\mathbf{x}, t) , \quad (4)$$

that is connected to the degree of Alfvénization of the system, i.e. to the presence of waves traveling in the direction of the mean global or local magnetic field (Dobrowolny et al. 1980; Biskamp 1993). In this paper we will focus on the importance of magnetic and kinetic helicities (helicities in short in what follows) for the growth rate of a large-scale magnetic field, always considering the case of almost vanishing cross helicity (see also the concluding remarks about possible generalization of our work to include also the latter). To be as simple as possible we will concentrate only on periodic and homogeneous conditions. The analytical and numerical work is based on the helical-Fourier decomposition developed for Navier-Stokes equations by the pioneering work of Waleffe (1992) and Constantin & Majda (1988). Such decomposition is exact and has led to an important breakthrough in the understanding of the entangled energy-helicity dynamics in three-dimensional Navier-Stokes turbulence (Waleffe 1992; Biferale & Titi 2013). It has been extended to MHD only recently (Lessinnes et al. 2009; Linkmann et al. 2016) and it promises to be a key tool also for problems where the physics is controlled by the interactions among magnetic/kinetic helical waves (Cho 2011; Galtier & Bhattacharjee 2003, 2005; Galtier & Meyrand 2014). Moreover, the helical-Fourier basis is also the natural decomposition to be used in numerical simulations, either to analyze the data or to perform explicit numerical experiments by projecting the equations on a given subset of Fourier modes, in order to highlight the physics of some particular interacting waves. This procedure has already been carried out for the Navier-Stokes equations with some surprising results (Biferale et al. 2012, 2013; Sahoo et al. 2015; Alexakis 2016) connected to the discovery of a subclass of (kinetic) helical modes transferring energy backwards in a fully 3D turbulent flow, i.e. the identification of those Fourier interactions responsible for the energy backscatter. Simulations of homogeneous magnetohydrodynamic turbulence in a periodic box without a background magnetic field have been used as prototypical systems to study the circumstances under which large-scale magnetic field growth occurs, such as the α -effect (Steenbeck et al. 1966; Brandenburg 2001) and the inverse cascade of magnetic helicity (Frisch et al. 1975; Pouquet et al. 1976; Balsara & Pouquet 1999; Brandenburg 2001; Alexakis et al. 2006; Müller et al. 2012; Malapaka & Müller 2013). Concerns have been raised in the literature about the effectiveness of the α -effect in generating large-scale magnetic fields with strong amplitude due to the detrimental feedback that fast-growing small-scale magnetic fields have on the growth rate of the large-scale magnetic field (Vainshtein & Cattaneo 1992; Cattaneo & Hughes 1996). This is the problem of catastrophic α -quenching, and much theoretical efforts have been made in order to find dynamo models which are able to circumvent this problem. In this paper we focus on the statistical and dynamical factors that might promote or deplete the growth of a large-scale magnetic field. We do it by using a systematic dissection of the three dimensional MHD equations in helical-Fourier modes as pioneered in (Linkmann et al. 2016). We first analyze the temporal evolution of three velocity and three magnetic helical-Fourier modes at wavenumbers, k, p, q , the basic brick of any quadratic non-linear transfer. Considering all helical combinations, there are 64 possible different subset of closed dynamical systems which represent the minimal backbone of interacting modes conserving all inviscid invariants. A graphical representation of such a basic system is given in Fig. 1. carried out by Linkmann et al. (2016), considering the most general equilibria. This led to the identification of linear instabilities that could be associated with forward and inverse transfer of total energy and magnetic helicity. Here we restrict our attention to equilibria and instabilities that can be connected to cases of astrophysical interest, i.e. kinematic dynamo regimes and inverse cascade effects. We further extend the analysis carried out in (Linkmann et al. 2016) by specifying the magnetic field growth rates (if any) and providing clear predictions on the expected helical signatures of the dominant instabilities. This enables us to link specific dynamical properties connected to the kinematic dynamo action and/or the inverse cascade of magnetic helicity with the geometrical structure of the triad (local versus non-local Fourier interactions) and with its kinematic contents (helicities). Interestingly, the entangled dynamics of velocity-magnetic fields is already extremely rich at the level of these most basic interactions.

The second part of the paper is devoted to develop for the first time a thoughtful numerical validation and benchmark of the previous theoretical analysis by Direct Numerical Simulation (DNS) of the full MHD equations with and without a small-scale forcing on the magnetic field. Forcing the magnetic field, allows us to switch from a situation where the magnetic field is initially in the kinematic dynamo regime to a case where Lorentz force is always acting at all scales, thanks to the strong injection of magnetic fluctuations. We always analyze velocity and magnetic fluctuations in terms of their helical-Fourier components such as to be able to directly match with the theoretical predictions based on the simplified single triad dynamics. We changed the helical properties of the magnetic forcing (when applied), such as to break mirror symmetry with different injection mechanisms. We study two different configurations, with large- or small-scale injection of kinetic energy and helicity, corresponding to turbulent or laminar regimes. Furthermore, we also present some ad-hoc simulations by restricting the dynamics of the velocity field to evolve only on modes with one given sign of helicity, which induces a strong breaking of mirror-symmetry already at the level of the equations of motion.

The combined analytical and numerical analysis lead to the following conclusions: (a) In presence of small-scale residual kinetic helicity and with an initially weak magnetic field, the large-scale magnetic field develops a helical signature of opposite sign with respect to the kinetic helicity, in agreement with the predictions of the classical α -effect in presence of scale-separation. (b) In the same flow configuration as in point (a), but with a strong injection of small-scale magnetic fluctuations, the growing large-scale magnetic field has the same sign of helicity as the injected helical small-scale magnetic fluctuations, a mechanism leading to an *inverse cascade of magnetic helicity* (Frisch et al. 1975). The two different behaviors are connected to two different properties of the single-triad dynamics. In case (a), the growth is α -like, due to the direct stretching of the magnetic lines by the helical velocity field. In case (b) the growth is dominated by purely non-linear effects due to the Lorentz force on the velocity field and by the stretching of the magnetic field by the velocity.

2. THEORETICAL AND ANALYTICAL RESULTS

We consider the MHD equations for incompressible flow

$$\partial_t \mathbf{u} = -\frac{1}{\rho} \nabla P - (\mathbf{u} \cdot \nabla) \mathbf{u} + \frac{1}{\rho} (\nabla \times \mathbf{b}) \times \mathbf{b} + \nu \Delta \mathbf{u} , \quad (5)$$

$$\partial_t \mathbf{b} = (\mathbf{b} \cdot \nabla) \mathbf{u} - (\mathbf{u} \cdot \nabla) \mathbf{b} + \eta \Delta \mathbf{b} , \quad (6)$$

$$\nabla \cdot \mathbf{u} = 0 \quad \text{and} \quad \nabla \cdot \mathbf{b} = 0 , \quad (7)$$

where \mathbf{u} denotes the velocity field, \mathbf{b} the magnetic induction expressed in Alfvén units, ν the kinematic viscosity, η the magnetic resistivity, P the pressure and ρ the density, which is set to unity for convenience. In the limit of vanishing viscosity and resistivity these equations conserve the magnetic helicity H_m , the cross-helicity H_c , and the total energy

$$E(t) = \frac{1}{2} \int_V d\mathbf{x} (|\mathbf{u}(\mathbf{x}, t)|^2 + |\mathbf{b}(\mathbf{x}, t)|^2) . \quad (8)$$

We consider eqs. (5)-(7) on a domain $[0, L]^3$ with periodic boundary conditions in order to assess scale-dependent dynamics by Fourier analysis. The Fourier transforms $\hat{\mathbf{u}}$ and $\hat{\mathbf{b}}$ of the velocity and magnetic field fluctuations evolve according to the following system of equations

$$(\partial_t + \nu k^2) \hat{\mathbf{u}}_{\mathbf{k}}(t) = \left(\mathbb{I} - \frac{\mathbf{k} \otimes \mathbf{k}}{k^2} \right) \left[\sum_{\mathbf{k}+\mathbf{p}+\mathbf{q}=0} \left(-i\mathbf{p} \times \hat{\mathbf{u}}_{\mathbf{p}}(t)^* \times \hat{\mathbf{u}}_{\mathbf{q}}(t)^* + (i\mathbf{p} \times \hat{\mathbf{b}}_{\mathbf{p}}(t))^* \times \hat{\mathbf{b}}_{\mathbf{q}}(t)^* \right) \right] , \quad (9)$$

$$(\partial_t + \eta k^2) \hat{\mathbf{b}}_{\mathbf{k}}(t) = i\mathbf{k} \times \sum_{\mathbf{k}+\mathbf{p}+\mathbf{q}=0} \hat{\mathbf{u}}_{\mathbf{p}}(t)^* \times \hat{\mathbf{b}}_{\mathbf{q}}(t)^* , \quad (10)$$

where $*$ denotes the complex conjugate. The inertial term $(\mathbf{u} \cdot \nabla) \mathbf{u}$ in the momentum equation (5) has been written in rotational form $(\mathbf{u} \cdot \nabla) \mathbf{u} = (\nabla \times \mathbf{u}) \times \mathbf{u} + \nabla |\mathbf{u}|^2 / 2$ and the pressure has been eliminated using the projector $P_{ij} = \delta_{ij} - k_i k_j / k^2$. Due to the statistical homogeneity of the vector field fluctuations, the structure of the vector field couplings in eq. (9) and eq. (10) are expressed by triadic interactions of wavevectors, a triad of wavevectors \mathbf{k} , \mathbf{p} and \mathbf{q} being defined by requiring $\mathbf{k} + \mathbf{p} + \mathbf{q} = 0$. In the following we study these triadic interactions with a view of extracting information on the effects of helicities on the dynamics of the magnetic field.

2.1. Helical decomposition

Being solenoidal vector fields, the Fourier transforms $\hat{\mathbf{u}}_{\mathbf{k}}$ and $\hat{\mathbf{b}}_{\mathbf{k}}$ are orthogonal to the wavevector \mathbf{k} and have only two degrees of freedom. These can be expressed by projection onto circularly polarized waves:

$$\hat{\mathbf{u}}_{\mathbf{k}}(t) = u_{\mathbf{k}}^+(t)\mathbf{h}_{\mathbf{k}}^+ + u_{\mathbf{k}}^-(t)\mathbf{h}_{\mathbf{k}}^- = \sum_{s_k} u_{\mathbf{k}}^{s_k}(t)\mathbf{h}_{\mathbf{k}}^{s_k}, \quad (11)$$

$$\hat{\mathbf{b}}_{\mathbf{k}}(t) = b_{\mathbf{k}}^+(t)\mathbf{h}_{\mathbf{k}}^+ + b_{\mathbf{k}}^-(t)\mathbf{h}_{\mathbf{k}}^- = \sum_{s_k} b_{\mathbf{k}}^{s_k}(t)\mathbf{h}_{\mathbf{k}}^{s_k}, \quad (12)$$

where $s_k = \pm$ and $\mathbf{h}_{\mathbf{k}}^{\pm}$ are the two fully helical orthonormal eigenvectors of the curl operator satisfying $i\mathbf{k} \times \mathbf{h}_{\mathbf{k}}^{s_k} = s_k k \mathbf{h}_{\mathbf{k}}^{s_k}$. The above decomposition was first proposed for the three-dimensional Navier-Stokes case in (Constantin & Majda 1988; Waleffe 1992) and later generalized for the MHD case in (Lessinnes et al. 2009; Linkmann et al. 2016). Similar decompositions have also been exploited to build up simplified models of turbulence (Lessinnes et al. 2009; De Pietro et al. 2015). Here we apply it, for the first time in a systematical way, to disentangle different basic transfers in the full MHD case. Since the helical basis vectors $\mathbf{h}_{\mathbf{k}}^{s_k}$ are time-independent, all information concerning the dynamics of the system is contained in the helical coefficients $u_{\mathbf{k}}^{s_k}(t)$ and $b_{\mathbf{k}}^{s_k}(t)$.

We can further decompose the kinetic and magnetic spectra in terms of their helical components as

$$E_u(k, t) = E_u^+(k, t) + E_u^-(k, t); \quad E_u^{\pm}(k, t) = \frac{1}{2} \sum_{|\mathbf{k}|=k} |u_{\mathbf{k}}^{\pm}(t)|^2 \quad (13)$$

$$E_b(k, t) = E_b^+(k, t) + E_b^-(k, t); \quad E_b^{\pm}(k, t) = \frac{1}{2} \sum_{|\mathbf{k}|=k} |b_{\mathbf{k}}^{\pm}(t)|^2. \quad (14)$$

The ideal invariants given by eqs. (1), (4) and (8) are conserved in single triad interactions (Lessinnes et al. 2009, 2011) and can be expressed as:

$$E(t) = \frac{1}{2} \sum_{\mathbf{k}} (|u_{\mathbf{k}}^+(t)|^2 + |u_{\mathbf{k}}^-(t)|^2 + |b_{\mathbf{k}}^+(t)|^2 + |b_{\mathbf{k}}^-(t)|^2), \quad (15)$$

$$H_m(t) = \sum_{\mathbf{k}} \frac{1}{k} (|b_{\mathbf{k}}^+(t)|^2 - |b_{\mathbf{k}}^-(t)|^2), \quad (16)$$

$$H_c(t) = \sum_{\mathbf{k}} \mathcal{R}(u_{\mathbf{k}}^+(t)b_{\mathbf{k}}^{+*}(t) + u_{\mathbf{k}}^-(t)b_{\mathbf{k}}^{-*}(t)), \quad (17)$$

where \mathcal{R} is the real part of a complex number. Similarly, the kinetic helicity becomes

$$H_k(t) = \sum_{\mathbf{k}} \hat{\mathbf{u}}(\mathbf{k}, t) \hat{\boldsymbol{\omega}}(-\mathbf{k}, t) = \sum_{\mathbf{k}} k (|u_{\mathbf{k}}^+(t)|^2 - |u_{\mathbf{k}}^-(t)|^2), \quad (18)$$

with $\hat{\boldsymbol{\omega}}(\mathbf{k}, t)$ being the Fourier transform of the vorticity. For conciseness we will drop the explicit notation of the time-dependence of the helical coefficients and the corresponding energy spectra from now on.

2.2. MHD-Helical dynamics

Inserting the exact decompositions (11-12) into (9-10) and taking the inner product with $\mathbf{h}_{\mathbf{k}}^{s_k}$ we obtain the helical-Fourier version of the MHD equations (Waleffe 1992; Lessinnes et al. 2009):

$$\begin{aligned} (\partial_t + \nu k^2) u_{\mathbf{k}}^{s_k*} &= \frac{1}{2} \sum_{\mathbf{k}+\mathbf{p}+\mathbf{q}=0} \sum_{s_p, s_q} g_{s_k s_p s_q}^{IN} (s_p p - s_q q) u_{\mathbf{p}}^{s_p} u_{\mathbf{q}}^{s_q} - \sum_{\sigma_p, \sigma_q} g_{s_k \sigma_p \sigma_q}^{LF} (\sigma_p p - \sigma_q q) b_{\mathbf{p}}^{\sigma_p} b_{\mathbf{q}}^{\sigma_q}, \\ (\partial_t + \eta k^2) b_{\mathbf{k}}^{\sigma_k*} &= \frac{\sigma_k k}{2} \sum_{\mathbf{k}+\mathbf{p}+\mathbf{q}=0} \sum_{\sigma_p, \sigma_q} g_{\sigma_k \sigma_p \sigma_q}^{M1} b_{\mathbf{p}}^{\sigma_p} u_{\mathbf{q}}^{s_q} - \sum_{s_p, \sigma_q} g_{\sigma_k s_p \sigma_q}^{M2} u_{\mathbf{p}}^{s_p} b_{\mathbf{q}}^{\sigma_q} \end{aligned} \quad (19)$$

where the coupling coefficients $g_{s_k s_p s_q}^{IN}$ and $g_{s_k \sigma_p \sigma_q}^{LF}$ originate from the inertial term and the Lorentz force in the momentum equation, respectively, while $g_{\sigma_k \sigma_p \sigma_q}^{M1}$ and $g_{\sigma_k s_p \sigma_q}^{M2}$ originate from the symmetrised induction equation. The coupling coefficients are given explicitly in eq. (A1) in Appendix A. It is very important to realize that the non-linear triadic interactions on the RHS of eq. (19) can be further decomposed into a subset of basic bricks consisting of three helical velocity and magnetic modes at wavevectors $\mathbf{p}, \mathbf{k}, \mathbf{q}$ such that $\mathbf{p} + \mathbf{k} + \mathbf{q} = 0$, characterized by one possible combination of chiral numbers $(s_k, s_p, s_q) = (\pm, \pm, \pm)$ for the velocity modes and $(\sigma_k, \sigma_p, \sigma_q) = (\pm, \pm, \pm)$ for the

magnetic modes as shown in Fig. 1:

$$\begin{aligned}
\partial_t u_{\mathbf{k}}^{s_k*} &= g_{s_k s_p s_q}^{IN} (s_p p - s_q q) u_{\mathbf{p}}^{s_p} u_{\mathbf{q}}^{s_q} - g_{s_k \sigma_p \sigma_q}^{LF} (\sigma_p p - \sigma_q q) b_{\mathbf{p}}^{\sigma_p} b_{\mathbf{q}}^{\sigma_q} , \\
\partial_t u_{\mathbf{p}}^{s_p*} &= g_{s_k s_p s_q}^{IN} (s_q q - s_k k) u_{\mathbf{q}}^{s_q} u_{\mathbf{k}}^{s_k} - g_{\sigma_k \sigma_p \sigma_q}^{LF} (\sigma_q q - \sigma_k k) b_{\mathbf{q}}^{\sigma_q} b_{\mathbf{k}}^{\sigma_k} , \\
\partial_t u_{\mathbf{q}}^{s_q*} &= g_{s_k s_p s_q}^{IN} (s_k k - s_p p) u_{\mathbf{k}}^{s_k} u_{\mathbf{p}}^{s_p} - g_{\sigma_k \sigma_p \sigma_q}^{LF} (\sigma_k k - \sigma_p p) b_{\mathbf{k}}^{\sigma_k} b_{\mathbf{p}}^{\sigma_p} , \\
\partial_t b_{\mathbf{k}}^{\sigma_k*} &= \sigma_k k \left(g_{\sigma_k \sigma_p \sigma_q}^{M1} b_{\mathbf{p}}^{\sigma_p} u_{\mathbf{q}}^{s_q} - g_{\sigma_k \sigma_p \sigma_q}^{M2} u_{\mathbf{p}}^{s_p} b_{\mathbf{q}}^{\sigma_q} \right) , \\
\partial_t b_{\mathbf{p}}^{\sigma_p*} &= \sigma_p p \left(g_{\sigma_k \sigma_p \sigma_q}^{M1} b_{\mathbf{q}}^{\sigma_q} u_{\mathbf{k}}^{s_k} - g_{\sigma_k \sigma_p \sigma_q}^{M2} u_{\mathbf{q}}^{s_q} b_{\mathbf{k}}^{\sigma_k} \right) , \\
\partial_t b_{\mathbf{q}}^{\sigma_q*} &= \sigma_q q \left(g_{\sigma_k \sigma_p \sigma_q}^{M1} b_{\mathbf{k}}^{\sigma_k} u_{\mathbf{p}}^{s_p} - g_{\sigma_k \sigma_p \sigma_q}^{M2} u_{\mathbf{k}}^{s_k} b_{\mathbf{p}}^{\sigma_p} \right) .
\end{aligned} \tag{20}$$

Considering the symmetry of the original equations for a global change of all positive helical waves into negative helical waves (mirror symmetry), we obtain 32 possible independent combinations of chiral interactions represented by eq. (20). Equation (20) thus describes a minimal triadic interaction (MTI), where minimal refers to the smallest number of degrees of freedom necessary to represent the structure of the quadratic couplings in the MHD equations. It is crucial to realize that each of these 32 MTI systems is closed in itself and that the energy, the magnetic helicity and the cross-helicity are exactly preserved for each system. A stability analysis of the above eq. (20) shows that all possible fixed points are given by non-zero entries at only one wavevector, say at \mathbf{p}_0 (Linkmann et al. 2016). We will denote these equilibria by $(B_{\mathbf{p}_0}^+, B_{\mathbf{p}_0}^-, U_{\mathbf{p}_0}^+, U_{\mathbf{p}_0}^-)$. Studying the stability of these equilibria yields information on possible energy/helicity transfers away from a given scale in the system, as shown for the Navier-Stokes case in (Kraichnan 1967; Waleffe 1992, 1993). In the absence of the magnetic field, the structure of the system of first-order ODEs describing a single triad is very similar to the Euler equations describing the torque-free rotation of a rigid body about its principal axes of inertia, and the stability analysis was carried out in (Waleffe 1992). The procedure remains conceptually the same for MHD with added complications due to a larger number of coupled dynamical variables and with the added value that one might gain some insight into the basic physical mechanisms governing kinematic dynamo action or into the effect of the Lorentz force on the flow. The stability analysis for the MHD case restricted to *homochiral* MTI system, i.e. interactions between the same chiral combination of velocity and magnetic fields $s_p = \sigma_p, s_q = \sigma_q, s_k = \sigma_k$, has been performed in (Linkmann et al. 2016). In this paper we perform a few important steps forward with respect to the analysis reported in (Linkmann et al. 2016). First, we will clarify under which circumstances the analysis by (Linkmann et al. 2016) is sufficient, i.e. where a distinction between homo- and heterochiral triads is relevant and where it is not required. Second, we will extend the results concerning kinematic dynamo action and the inverse magnetic helicity cascade in order to deliver qualitatively testable predictions. Finally, in Sec. 4 we will perform a direct benchmark of all predictions by performing high resolutions DNS of the full MHD equations and exploiting the helical decomposition to rationalize the numerical results.

2.2.1. Stability analysis of a general MTI system

Let us first fix the notation. We always consider the following order for wavenumbers:

$$k < q < p.$$

As a result whenever we want to address the growth of perturbations at small wavenumbers (large scales), we will take the equilibria for magnetic or velocity field at the largest wavenumber (smallest scale) $p_0 = |\mathbf{p}_0|$. Viceversa, for the growth of perturbations at large wavenumbers (small scales) we will fix the equilibria at the smallest wavenumber (largest scale) $k_0 = |\mathbf{k}_0|$. Up to first order, the evolution equations of the large-scale perturbations, $\tilde{u}_{\mathbf{k}}^{s_k}, \tilde{u}_{\mathbf{q}}^{s_q}, \tilde{b}_{\mathbf{k}}^{\sigma_k}$ and $\tilde{b}_{\mathbf{q}}^{\sigma_q}$ are:

$$\text{Large Scale} \left\{ \begin{aligned}
\partial_t \tilde{u}_{\mathbf{k}}^{s_k*} &= g_{s_k s_{p_0} s_q}^{IN} (s_p p_0 - s_q q) U_{\mathbf{p}_0}^{s_{p_0}} \tilde{u}_{\mathbf{q}}^{s_q} - g_{s_k \sigma_{p_0} \sigma_q}^{LF} (\sigma_{p_0} p_0 - \sigma_q q) B_{\mathbf{p}_0}^{\sigma_{p_0}} \tilde{b}_{\mathbf{q}}^{\sigma_q} , \\
\partial_t \tilde{u}_{\mathbf{q}}^{s_q*} &= g_{s_k s_{p_0} s_q}^{IN} (s_k k - s_{p_0} p_0) \tilde{u}_{\mathbf{k}}^{s_k} U_{\mathbf{p}_0}^{s_{p_0}} - g_{\sigma_k \sigma_{p_0} \sigma_q}^{LF} (\sigma_k k - \sigma_{p_0} p_0) \tilde{b}_{\mathbf{k}}^{\sigma_k} B_{\mathbf{p}_0}^{\sigma_{p_0}} , \\
\partial_t \tilde{b}_{\mathbf{k}}^{\sigma_k*} &= \sigma_k k \left(g_{\sigma_k \sigma_{p_0} \sigma_q}^{M1} B_{\mathbf{p}_0}^{\sigma_{p_0}} \tilde{u}_{\mathbf{q}}^{s_q} - g_{\sigma_k \sigma_{p_0} \sigma_q}^{M2} U_{\mathbf{p}_0}^{s_{p_0}} \tilde{b}_{\mathbf{q}}^{\sigma_q} \right) , \\
\partial_t \tilde{b}_{\mathbf{q}}^{\sigma_q*} &= \sigma_q q \left(g_{\sigma_k \sigma_{p_0} \sigma_q}^{M1} \tilde{b}_{\mathbf{k}}^{\sigma_k} U_{\mathbf{p}_0}^{s_{p_0}} - g_{\sigma_k \sigma_{p_0} \sigma_q}^{M2} \tilde{u}_{\mathbf{k}}^{s_k} B_{\mathbf{p}_0}^{\sigma_{p_0}} \right) ,
\end{aligned} \right.$$

while for the evolution of small-scale perturbations $\tilde{u}_{\mathbf{p}}^{s_p}$, $\tilde{u}_{\mathbf{q}}^{s_q}$, $\tilde{b}_{\mathbf{p}}^{\sigma_p}$ and $\tilde{b}_{\mathbf{q}}^{\sigma_q}$ we have:

$$\text{Small Scale} \begin{cases} \partial_t \tilde{u}_{\mathbf{p}}^{s_p*} &= g_{s_{k_0} s_p s_q}^{IN} (s_q q - s_{k_0} k_0) \tilde{u}_{\mathbf{q}}^{s_q} U_{\mathbf{k}_0}^{s_{k_0}} - g_{\sigma_{k_0} s_p \sigma_q}^{LF} (\sigma_q q - \sigma_{k_0} k_0) \tilde{b}_{\mathbf{q}}^{\sigma_q} B_{\mathbf{k}_0}^{\sigma_{k_0}}, \\ \partial_t \tilde{u}_{\mathbf{q}}^{s_q*} &= g_{s_{k_0} s_p s_q}^{IN} (s_{k_0} k_0 - s_p p) U_{\mathbf{k}_0}^{s_{k_0}} \tilde{u}_{\mathbf{p}}^{s_p} - g_{\sigma_{k_0} \sigma_p \sigma_q}^{LF} (\sigma_{k_0} k_0 - \sigma_p p) B_{\mathbf{k}_0}^{\sigma_{k_0}} \tilde{b}_{\mathbf{p}}^{\sigma_p}, \\ \partial_t \tilde{b}_{\mathbf{p}}^{\sigma_p*} &= \sigma_p p \left(g_{s_{k_0} \sigma_p \sigma_q}^{M1} \tilde{b}_{\mathbf{q}}^{\sigma_q} U_{\mathbf{k}_0}^{s_{k_0}} - g_{\sigma_{k_0} \sigma_p \sigma_q}^{M2} \tilde{u}_{\mathbf{q}}^{s_q} B_{\mathbf{k}_0}^{\sigma_{k_0}} \right), \\ \partial_t \tilde{b}_{\mathbf{q}}^{\sigma_q*} &= \sigma_q q \left(g_{s_{k_0} s_p \sigma_q}^{M1} B_{\mathbf{k}_0}^{\sigma_{k_0}} \tilde{u}_{\mathbf{p}}^{s_p} - g_{s_{k_0} \sigma_p \sigma_q}^{M2} U_{\mathbf{k}_0}^{s_{k_0}} \tilde{b}_{\mathbf{p}}^{\sigma_p} \right). \end{cases}$$

In the following we will address only fully kinetic helical equilibria ($B_{\mathbf{p}_0}^{\pm} = 0, U_{\mathbf{p}_0}^{-} = 0, U_{\mathbf{p}_0}^{+} \neq 0$) or fully magnetic helical equilibria ($U_{\mathbf{p}_0}^{\pm} = 0, B_{\mathbf{p}_0}^{-} = 0, B_{\mathbf{p}_0}^{+} \neq 0$). In order to assess the linear stability of a given equilibrium solution of each single set of coupled first-order ODEs describing an individual MTI system, a further differentiation in time is required leading to four coupled second-order ODEs. The procedure is explained in full detail in (Waleffe 1992) for purely inertial dynamics and in (Linkmann et al. 2016) for MHD. Here we will consider the stability properties of a given equilibrium for each of the 32 MTI closed sub-systems for both large- or small-scale equilibria, and we will discuss the stability properties of the equilibrium as a function of the helical (magnetic or kinetic) content of the equilibrium and the perturbations. The exponential growth of a given perturbation is associated with transfers from the equilibrium mode into the perturbing modes. For example, kinematic dynamo action can be represented by the growth of a magnetic perturbation starting from a mechanical equilibrium given by ($B_{\mathbf{p}_0}^{\pm} = U_{\mathbf{p}_0}^{-} = 0, U_{\mathbf{p}_0}^{+} \neq 0$), while the feedback of the Lorentz force on the fluid can be quantified by the dynamics of the velocity perturbation starting from a magnetic helical equilibrium ($U_{\mathbf{p}_0}^{\pm} = B_{\mathbf{p}_0}^{-} = 0, B_{\mathbf{p}_0}^{+} \neq 0$).

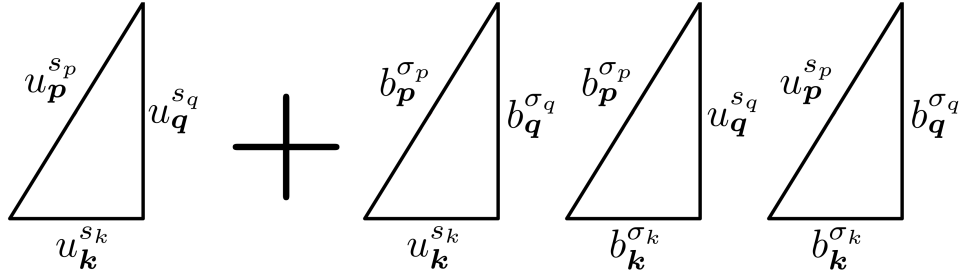
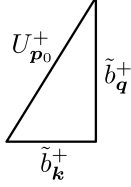


Figure 1. Graphical representation of the minimal non-linear system consisting of the coupling among a velocity (left) and a magnetic-velocity (right) triadic interaction. The magnetic-velocity interaction corresponds to several terms in Eq. (20), depending on whether the time evolution of the velocity field mode or the magnetic modes is considered.

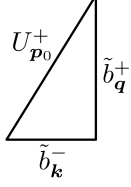
3. SUMMARY OF PREDICTIONS

3.1. Large scale kinematic dynamo

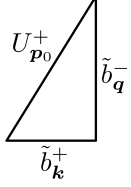
In order to study large-scale kinematic dynamo action restricted to each one of the 32 MTI system separately, we start from a fully helical mechanical equilibrium at the smallest scale, subject to magnetic perturbation at larger scales. Following the notation introduced in the previous section, this corresponds to an equilibrium at wavevector \mathbf{p}_0 given by ($B_{\mathbf{p}_0}^{+} = 0, B_{\mathbf{p}_0}^{-} = 0, U_{\mathbf{p}_0}^{+} \neq 0, U_{\mathbf{p}_0}^{-} = 0$) subject to magnetic perturbations $\tilde{b}_{\mathbf{k}}^{+}$, $\tilde{b}_{\mathbf{k}}^{-}$, $\tilde{b}_{\mathbf{q}}^{+}$ and $\tilde{b}_{\mathbf{q}}^{-}$, where $p_0 > q > k$. Given the particular equilibrium, one can show from eq. (21) that it is sufficient to consider 4 classes only: Due to the choice of the equilibrium the 32 MTI systems reduce to 16, which is further reduced to 4 as we only consider the evolution of the magnetic perturbations. Thus the only possibilities are given by all combinations ($\sigma_k, s_{p_0} = +, \sigma_q$), and we recover the set of minimal triadic interactions connected to kinematic dynamo action in (Linkmann et al. 2016). Note that the distinction between homo- and heterochiral MTI systems is not relevant here, as only magnetic perturbations to a mechanical equilibrium are considered. Even if mechanical perturbations were considered, the evolution of the magnetic perturbations does not depend on the helicity content of the mechanical perturbations as they do not couple. In the following, for the sake of completeness we first recapitulate the known results on triadic dynamo action (Linkmann et al. 2016) and subsequently extend the analysis in order to supply qualitative predictions concerning the growth rates. The evolution equations of the perturbations for each of the 4 individual MTI systems are:



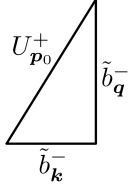
$$D1 \quad \begin{cases} \partial_t |\tilde{b}_k^+|^2 = -k g_{++++}^{M2} \tilde{b}_k^{+*} U_{p0}^+ \tilde{b}_q^+ + \text{c. c.} , \\ \partial_t |\tilde{b}_q^+|^2 = q g_{++++}^{M1} \tilde{b}_q^{+*} \tilde{b}_k^+ U_{p0}^+ + \text{c. c.} , \end{cases} \quad (21)$$



$$D2 \quad \begin{cases} \partial_t |\tilde{b}_k^+|^2 = -k g_{++++}^{M2} \tilde{b}_k^{+*} U_{p0}^+ \tilde{b}_q^- + \text{c. c.} , \\ \partial_t |\tilde{b}_q^-|^2 = -q g_{++++}^{M1} \tilde{b}_q^{-*} \tilde{b}_k^+ U_{p0}^+ + \text{c. c.} , \end{cases} \quad (22)$$



$$D3 \quad \begin{cases} \partial_t |\tilde{b}_k^-|^2 = k g_{-+++}^{M2} \tilde{b}_k^{-*} U_{p0}^+ \tilde{b}_q^+ + \text{c. c.} , \\ \partial_t |\tilde{b}_q^+|^2 = q g_{-+++}^{M1} \tilde{b}_q^{+*} \tilde{b}_k^- U_{p0}^+ + \text{c. c.} , \end{cases} \quad (23)$$



$$D4 \quad \begin{cases} \partial_t |\tilde{b}_k^-|^2 = k g_{-+-}^{M2} \tilde{b}_k^{-*} U_{p0}^+ \tilde{b}_q^- + \text{c. c.} , \\ \partial_t |\tilde{b}_q^-|^2 = -q g_{-+-}^{M1} \tilde{b}_q^{-*} \tilde{b}_k^- U_{p0}^+ + \text{c. c.} , \end{cases} \quad (24)$$

where c. c. denotes the complex conjugate, and we have written the evolution equations in terms of the magnetic energy in order to highlight the structure of the different helical interactions D1-D4. The second-order equations governing magnetic field growth at \mathbf{k} and \mathbf{q} become for this particular equilibrium case:

$$D1 \quad \begin{cases} \partial_t^2 \tilde{b}_k^+ = -g_{++++}^{M2} g_{++++}^{M1*} kq |U_{p0}^+|^2 \tilde{b}_k^+ , \\ \partial_t^2 \tilde{b}_q^+ = -g_{++++}^{M1} g_{++++}^{M2*} kq |U_{p0}^+|^2 \tilde{b}_q^+ , \end{cases} \quad (25)$$

$$D2 \quad \begin{cases} \partial_t^2 \tilde{b}_k^+ = g_{+--+}^{M2} g_{+--+}^{M1*} kq |U_{p0}^+|^2 \tilde{b}_k^+ & U_{p0}^+ \xrightarrow{\tilde{b}_q^-} \tilde{b}_k^+ , \\ \partial_t^2 \tilde{b}_q^- = g_{+--+}^{M1} g_{+--+}^{M2*} kq |U_{p0}^+|^2 \tilde{b}_q^- & U_{p0}^+ \xrightarrow{\tilde{b}_k^+} \tilde{b}_q^- , \end{cases} \quad (26)$$

$$D3 \quad \begin{cases} \partial_t^2 \tilde{b}_k^- = g_{-+++}^{M2} g_{-+++}^{M1*} kq |U_{p0}^+|^2 \tilde{b}_k^- & U_{p0}^+ \xrightarrow{\tilde{b}_q^+} \tilde{b}_k^- , \\ \partial_t^2 \tilde{b}_q^+ = g_{-+++}^{M1} g_{-+++}^{M2*} kq |U_{p0}^+|^2 \tilde{b}_q^+ & U_{p0}^+ \xrightarrow{\tilde{b}_k^-} \tilde{b}_q^+ , \end{cases} \quad (27)$$

$$D4 \quad \begin{cases} \partial_t^2 \tilde{b}_k^- = -g_{-+-}^{M2} g_{-+-}^{M1*} kq |U_{p0}^+|^2 \tilde{b}_k^- , \\ \partial_t^2 \tilde{b}_q^- = -g_{-+-}^{M1} g_{-+-}^{M2*} kq |U_{p0}^+|^2 \tilde{b}_q^- . \end{cases} \quad (28)$$

From the definition of the coupling coefficients given by eq. (A1) and from the structure of the products shown in eq. A2 in Appendix A it is immediate to realize that the prefactors in front of the fluctuating fields in eqs. (25)-(27) are positive for classes D2 and D3 while they are negative for classes D1 and D4. Triadic dynamo action is therefore described by processes D2 and D3. The arrows in eqs. (26) and (27) indicate the transfer direction associated among the two fields and the superscripts indicate the ‘catalyzer’ mode. In both processes the magnetic perturbations are of opposite helicity, therefore we state the first observation:

(i) *Magnetic field perturbations of mutually opposite helicity are necessary to enable dynamo action* (Linkmann et al. 2016).

Having summarised the known results, we now proceed to a qualitative analysis of the growth rates. It is important to stress that at the largest scale, $1/k$, the magnetic fluctuation with helicity opposite to the one of the stretching

velocity field grows faster, because the ratio between the growth rates for processes D2 and D3 is given by

$$\left(\frac{g_{+++}^{M2} g_{+++}^{M1*}}{g_{-++}^{M2} g_{-++}^{M1*}}\right)^{1/2} = \frac{|k + p_0 - q|}{|-k + p_0 + q|} < 1. \quad (29)$$

as can be seen from eq. A5. Therefore this is leading to an α -like dynamo process, and we can make the second important observation:

(ii) *The main instability leading to large-scale dynamo action is of α -type.*

Moreover, we notice that the growth becomes more and more of α -type if the geometry of the triad is strongly non-local, i.e. $k \ll p_0 \simeq q$, because then $(g_{+++}^{M2} g_{+++}^{M1*}/g_{-++}^{M2} g_{-++}^{M1*})^{1/2} \rightarrow 0$, as can be seen from eq. (29). Our predictions for the large-scale dynamo are summarized in Fig. 2.

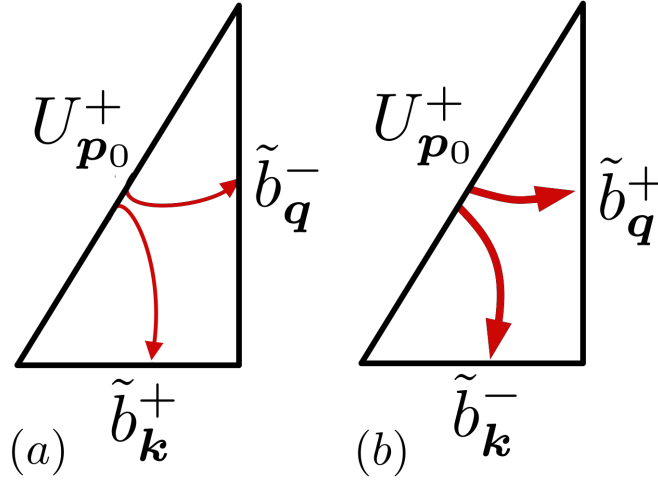


Figure 2. Summary of large-scale dynamo processes $D2 : U_{p_0}^+ \xrightarrow{\tilde{b}_q^-} \tilde{b}_k^+$ (a) and $D3 : U_{p_0}^+ \xrightarrow{\tilde{b}_q^+} \tilde{b}_k^-$ (b). The thickness of the arrows indicates the qualitative value of the growth rate.

3.2. Small scale kinematic dynamo

We now consider a mechanical equilibrium ($B_{k_0}^+ = 0, B_{k_0}^- = 0, U_{k_0}^+ \neq 0, U_{k_0}^-$) at the largest scale, which corresponds to the smallest wavenumber k_0 and study magnetic perturbations $\tilde{b}_p^+, \tilde{b}_p^-, \tilde{b}_q^+$ and \tilde{b}_q^- at smaller scales, i.e. at larger wavenumbers with $p > q > k_0$. The evolution of the magnetic energy for each of the four individual MTI systems are:

$$D1 \quad \begin{cases} \partial_t |\tilde{b}_p^+|^2 &= -p g_{+++}^{M1} \tilde{b}_p^+ \tilde{b}_q^+ U_{k_0}^+ + \text{c. c.}, \\ \partial_t |\tilde{b}_q^+|^2 &= q g_{+++}^{M2} \tilde{b}_q^+ U_{k_0}^+ \tilde{b}_p^+ + \text{c. c.}, \end{cases} \quad (30)$$

$$D2 \quad \begin{cases} \partial_t |\tilde{b}_p^+|^2 &= -p g_{+++}^{M1} \tilde{b}_p^+ \tilde{b}_q^- U_{k_0}^+ + \text{c. c.}, \\ \partial_t |\tilde{b}_q^-|^2 &= -q g_{+++}^{M2} \tilde{b}_q^- U_{k_0}^+ \tilde{b}_p^+ + \text{c. c.}, \end{cases} \quad (31)$$

$$D3 \quad \begin{cases} \partial_t |\tilde{b}_p^-|^2 &= p g_{+-+}^{M1} \tilde{b}_p^- \tilde{b}_q^+ U_{k_0}^+ + \text{c. c.}, \\ \partial_t |\tilde{b}_q^+|^2 &= q g_{+-+}^{M2} \tilde{b}_q^+ U_{k_0}^+ \tilde{b}_p^- + \text{c. c.}, \end{cases} \quad (32)$$

$$D4 \quad \begin{cases} \partial_t |\tilde{b}_p^-|^2 &= p g_{+-+}^{M1} \tilde{b}_p^- \tilde{b}_q^- U_{k_0}^+ + \text{c. c.}, \\ \partial_t |\tilde{b}_q^-|^2 &= -q g_{+-+}^{M2} \tilde{b}_q^- U_{k_0}^+ \tilde{b}_p^- + \text{c. c.}, \end{cases} \quad (33)$$

from which we derive the second-order equations

$$D1 \quad \begin{cases} \partial_t^2 \tilde{b}_p^+ &= -g_{++++}^{M1} g_{++++}^{M2*} pq |U_{\mathbf{k}_0}^+|^2 \tilde{b}_p^+ , \\ \partial_t^2 \tilde{b}_q^+ &= -g_{++++}^{M2} g_{++++}^{M1*} pq |U_{\mathbf{k}_0}^+|^2 \tilde{b}_q^+ , \end{cases} \quad (34)$$

$$D2 \quad \begin{cases} \partial_t^2 \tilde{b}_p^+ &= g_{+++-}^{M1} g_{+++-}^{M2*} pq |U_{\mathbf{k}_0}^+|^2 \tilde{b}_p^+ & U_{\mathbf{k}_0}^+ \xrightarrow{\tilde{b}_q^-} \tilde{b}_p^+ , \\ \partial_t^2 \tilde{b}_q^+ &= g_{+++-}^{M2} g_{+++-}^{M1*} pq |U_{\mathbf{k}_0}^+|^2 \tilde{b}_q^+ & U_{\mathbf{k}_0}^+ \xrightarrow{\tilde{b}_p^+} \tilde{b}_q^+ , \end{cases} \quad (35)$$

$$D3 \quad \begin{cases} \partial_t^2 \tilde{b}_p^- &= g_{+--+}^{M1} g_{+--+}^{M2*} pq |U_{\mathbf{k}_0}^+|^2 \tilde{b}_p^- & U_{\mathbf{k}_0}^+ \xrightarrow{\tilde{b}_q^+} \tilde{b}_p^- , \\ \partial_t^2 \tilde{b}_q^+ &= g_{+--+}^{M2} g_{+--+}^{M1*} pq |U_{\mathbf{k}_0}^+|^2 \tilde{b}_q^+ & U_{\mathbf{k}_0}^+ \xrightarrow{\tilde{b}_p^-} \tilde{b}_q^+ , \end{cases} \quad (36)$$

$$D4 \quad \begin{cases} \partial_t^2 \tilde{b}_p^- &= -g_{+--+}^{M1} g_{+--+}^{M2*} pq |U_{\mathbf{k}_0}^+|^2 \tilde{b}_p^- , \\ \partial_t^2 \tilde{b}_q^- &= -g_{+--+}^{M2} g_{+--+}^{M1*} pq |U_{\mathbf{k}_0}^+|^2 \tilde{b}_q^- . \end{cases} \quad (37)$$

Similar to the analysis of large-scale dynamo action, the prefactors in front of the fluctuations are positive for classes D2 and D3 while they are negative for classes D1 and D4. The growth of the small-scale magnetic field due to a large-scale velocity field is therefore also described by processes D2 and D3. However, we observe an important difference compared to the large-scale dynamo: Now, at the largest wavenumber, p , the magnetic fluctuation with the *same* helicity of the stretching velocity field has the larger growth rate, because

$$\left(\frac{g_{+++-}^{M1} g_{+++-}^{M2*}}{g_{+--+}^{M1} g_{+--+}^{M2*}} \right)^{1/2} = \frac{|k_0 + p - q|}{|k_0 - p + q|} > 1. \quad (38)$$

as can be seen from eq. (A6). Therefore we expect the opposite helical signature compared to the large-scale dynamo, that is:

(iii) *the growth of the magnetic field at scales smaller than the characteristic scale of the flow will mainly have the same helicity as the flow.*

By comparison of the ratio between the two growth rates for processes D2 and D3 we also observe that the small-scale dynamo operates more locally, because the growth rates diminish in both cases if the geometry of the triad is strongly non-local, i.e. for $k_0 \ll p \simeq q$ we obtain $(g_{+++-}^{M1} g_{+++-}^{M2*})^{1/2} \rightarrow 0$ and $(g_{+--+}^{M1} g_{+--+}^{M2*})^{1/2} \rightarrow 0$ as can be seen from (38). Our predictions for the small-scale dynamo are summarized in Fig. 3.

In conclusion, there are four possible classes of triad-by-triad dynamo action, out of which two classes correspond to large-scale dynamo action and two classes to small-scale dynamo action. For the large-scale dynamo one class has the same helical signature as the α -effect (Linkmann et al. 2016), this is class D3 given in eq. (27) and depicted in Fig. 2 (b). The other class, D2, which is described in eq. (26) and depicted in Fig. 2 (a), has the opposite helical signature. Most importantly, the α -like dynamo has the larger growth rate. Conversely, the two classes corresponding to the small-scale dynamo are shown in Fig. 3(a-b) and described in eqs. (35) and (36). At scales smaller than the characteristic scale of the mechanical equilibrium, class D2 mainly amplifies magnetic field perturbations with the same sign of helicity as the flow, while class D3 amplifies magnetic field modes with the opposite sign of helicity as the flow, and we found that class D2 has the larger growth rate compared to D3. The combination of the two classes of dynamo action with the larger growth rate, i.e. the combination of the α -like large-scale D3 with the small-scale D2, produces a helical signature consistent with the Stretch-Twist-Fold (STF) mechanism (Vainshtein & Zeldovich 1972; Childress & Gilbert 1995; Mininni 2011) of dynamo action in a positively helical flow: Negative magnetic helicity is generated at the large scales while positive magnetic helicity is generated at the small scales. The main result from the theoretical analysis of triad-by-triad dynamo action can therefore be summarized in the following statement:

(iv) *The dominant linear instabilities present in the basic triadic dynamics lead to dynamo action with the same helical signature as the STF-mechanism.* We point out that since in full MHD all modes interact, it yet remains to be seen to what extent the MTI dynamos D2 and D3 are representative of the full dynamics. We will address this point in Sec. 4.1.

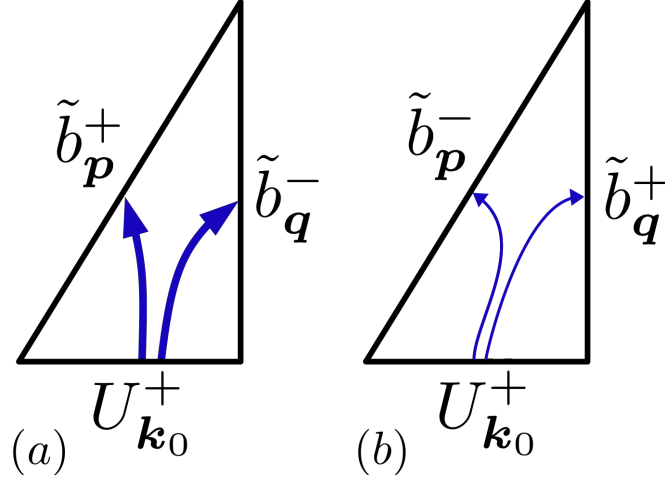


Figure 3. Summary of small-scale dynamo processes $D2 : U_{\mathbf{k}_0}^+ \xrightarrow{\tilde{b}_q^-} \tilde{b}_p^+$ (a) and $D3 : U_{\mathbf{k}_0}^+ \xrightarrow{\tilde{b}_q^+} \tilde{b}_p^-$ (b). The thickness of the arrows indicates the qualitative value of the growth rate.

3.3. Inverse cascade of magnetic helicity

In a strongly magnetized flow the magnetic field interacts with itself due to its back-reaction on the flow by the Lorentz force. In order to assess this interaction we consider a positively helical magnetic equilibrium ($B_{\mathbf{p}_0}^+ \neq 0, B_{\mathbf{p}_0}^- = U_{\mathbf{p}_0}^- = U_{\mathbf{p}_0}^+ = 0$) subject to magnetic and mechanical perturbations. Unlike for the kinematic dynamo, now the magnetic and mechanical perturbations couple, i.e. the inverse cascade and the effect of the Lorentz force are described by the same MTI system coupling the two effects. The latter implies that the distinction between homo- and heterochiral MTI systems is relevant if both processes are to be analysed. However, concerning the *existence* of linear instabilities the analysis can be simplified by restricting the focus on the inverse cascade and leaving the effect of the Lorentz force on the flow aside. Then it suffices to consider only one type of interaction by fixing the magnetic and mechanical perturbations at a given wavenumber each, and it is not necessary to further distinguish between homo- and heterochiral systems. For simplicity we only consider magnetic perturbations at the smallest wavenumber k in the triad and mechanical perturbations at the intermediate wavenumber q . The analysis of the 32 possible MTIs can then be reduced to the study of 4 individual MTIs by a similar argument as applied to the kinematic dynamo. This allows us to briefly summarise the known results on the inverse cascade (Linkmann et al. 2016) and to outline the main points. The evolution equations for the magnetic and mechanical perturbations $\tilde{b}_k^+, \tilde{b}_k^-, \tilde{u}_q^+$ and \tilde{u}_q^- are:

$$IC1 \quad \begin{cases} \partial_t |\tilde{b}_k^+|^2 = kg_{++++}^{M1} \tilde{b}_k^{+*} B_{\mathbf{p}_0}^+ \tilde{u}_q^+ + c. c. , \\ \partial_t |\tilde{u}_q^+|^2 = -g_{++++}^{LF} (k - p_0) \tilde{u}_q^{+*} B_{\mathbf{p}_0}^+ \tilde{b}_k^+ + c. c. , \end{cases} \quad (39)$$

$$IC2 \quad \begin{cases} \partial_t |\tilde{b}_k^+|^2 = kg_{+++-}^{M1} \tilde{b}_k^{+*} B_{\mathbf{p}_0}^+ \tilde{u}_q^- + c. c. , \\ \partial_t |\tilde{u}_q^-|^2 = -g_{+++-}^{LF} (k - p_0) \tilde{u}_q^{-*} B_{\mathbf{p}_0}^+ \tilde{b}_k^+ + c. c. , \end{cases} \quad (40)$$

$$IC3 \quad \begin{cases} \partial_t |\tilde{b}_k^-|^2 = -kg_{-+++}^{M1} \tilde{b}_k^{-*} B_{\mathbf{p}_0}^+ \tilde{u}_q^+ + c. c. , \\ \partial_t |\tilde{u}_q^+|^2 = -g_{-+++}^{LF} (-k - p_0) \tilde{u}_q^{+*} B_{\mathbf{p}_0}^+ \tilde{b}_k^- + c. c. , \end{cases} \quad (41)$$

$$IC4 \quad \begin{cases} \partial_t |\tilde{b}_k^-|^2 = -kg_{-+-}^{M1} \tilde{b}_k^{-*} B_{\mathbf{p}_0}^+ \tilde{u}_q^- + c. c. , \\ \partial_t |\tilde{u}_q^-|^2 = -g_{-+-}^{LF} (-k - p_0) \tilde{u}_q^{-*} B_{\mathbf{p}_0}^+ \tilde{b}_k^- + c. c. , \end{cases} \quad (42)$$

where again each equation describes the dynamics of one particular MTI system. Since this section is concerned with the dynamics of the magnetic field, we focus on the second-order evolution equations of the magnetic perturbations

only:

$$IC1 \quad \partial_t^2 \tilde{b}_k^+ = -g_{+++}^{M1} g_{+++}^{LF*} k(k-p_0) |B_{p_0}^+|^2 \tilde{b}_k^+ \quad B_{p_0}^+ \xrightarrow{\tilde{u}_q^+} \tilde{b}_k^+, \quad (43)$$

$$IC2 \quad \partial_t^2 \tilde{b}_k^+ = -g_{++-}^{M1} g_{++-}^{LF*} k(k-p_0) |B_{p_0}^+|^2 \tilde{b}_k^+ \quad B_{p_0}^+ \xrightarrow{\tilde{u}_q^-} \tilde{b}_k^+, \quad (44)$$

$$IC3 \quad \partial_t^2 \tilde{b}_k^- = -g_{-++}^{M1} g_{-++}^{LF*} k(k+p_0) |B_{p_0}^+|^2 \tilde{b}_k^-, \quad (45)$$

$$IC4 \quad \partial_t^2 \tilde{b}_k^- = -g_{-+-}^{M1} g_{-+-}^{LF*} k(k+p_0) |B_{p_0}^+|^2 \tilde{b}_k^-. \quad (46)$$

Again we consider under which circumstances linear instabilities occur. The products of coupling coefficients in eqs. (43)-(46) are always positive, hence we observe that the prefactors on RHS of the evolution equations for the negatively helical magnetic perturbations (eq. (45) and eq. (46)) are always negative, while the corresponding prefactors in the evolution equations for the positively helical magnetic perturbations (eq. (43) and eq. (44)) are positive because we chose $k < p_0$. We immediately see that:

(v) *a positively helical magnetic equilibrium at a given scale can only be unstable with respect to positively helical magnetic perturbations at larger scales (Linkmann et al. 2016).*

Since the magnetic perturbation and the equilibrium are of like-signed helicity this linear instability can be identified with the inverse cascade of magnetic helicity, by which magnetic helicity of one sign is transported from smaller to larger scales.

We point out that the terms on the RHS of eqs. (43) and (46) are essentially nonlinear, because their derivation required the coupling of the momentum and induction equations due to the Lorentz force as can be seen by the occurrence of the Lorentz coupling factors g^{LF} in eqs. (43) and (46). The coupling between the momentum and induction equations which is the only nonlinear contribution to the evolution of the magnetic field is therefore still present. Equations (43) and (44) thus describe a nonlinear contribution to the interscale energy transfer due to \mathbf{b} acting on \mathbf{u} which is acting back on \mathbf{b} : $\mathbf{b} \rightarrow \mathbf{u} \rightarrow \mathbf{b}$. That is, care has to be taken in the graphical representation and the physical interpretation of eqs. (43) and (44) as it may be tempting to associate linear instabilities with purely magnetic energy transfer due to advection by the velocity field: $\mathbf{b} \rightarrow \mathbf{b}$.

There are two classes of MTIs which have a linear instability associated with the inverse cascade of magnetic helicity, IC1 and IC2, where the IC1 describes the evolution of a positively magnetic field in a positively helical flow, because the catalyzer mode u_q^+ is positively helical, while the IC2 describes the evolution of a positively helical magnetic field in a negatively helical flow. By comparison of the respective growth rates we can assess in which situation the inverse cascade of magnetic helicity is most efficient. According to the discussion in Appendix A, we obtain

$$\left(\frac{g_{++-}^{M1} - g_{++-}^{LF*}}{g_{+++}^{M1} g_{+++}^{LF*}} \right)^{1/2} = \frac{|k + p_0 - q|}{|k + p_0 + q|} < 1. \quad (47)$$

that is, IC1 leads to a larger growth rate for the large-scale magnetic perturbation than IC2. Therefore we conclude that:

(vi) *the inverse cascade of magnetic helicity is more efficient in a helical flow where magnetic and kinetic helicity are of the same sign than in a helical flow where magnetic and kinetic helicity are of opposite sign.*

These results are summarized in Fig. 4. Furthermore, we note that IC2-transfers are more local than IC1-transfers, because for strongly nonlocal triads $k \ll p_0 \simeq q$ the combination of coupling factors $g_{+++}^{M1} g_{+++}^{LF*}$ corresponding to IC2 tends to zero, as can be seen from eq. (47).

4. NUMERICAL RESULTS

The analysis carried out in the previous sections is based on a simplified single-triad dynamics which cannot be the end of the story (Moffatt 2014). During the non-linear evolution of the whole set of triads in the full MHD equations different instabilities due to different triad shapes and helical content of the corresponding MTIs will superpose and interact. Therefore, it is not trivial to predict the behavior of the full system and the typical transfer that will dominate in the fully coupled MHD regime. A paradigmatic example is given by the case of the Navier-Stokes equations in absence of the magnetic field (Biferale et al. 2012; Biferale & Titi 2013; Biferale et al. 2013). There, we know that one set of

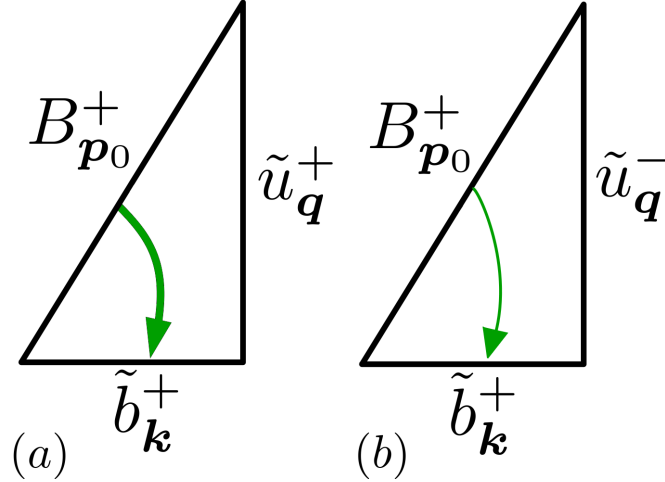


Figure 4. Summary of inverse transfer processes $IC1 : B_{p_0}^+ \xrightarrow{\tilde{u}_q^+} \tilde{b}_k^+$ (a) and $IC2 : B_{p_0}^+ \xrightarrow{\tilde{u}_q^-} \tilde{b}_k^+$ (b). The thickness of the arrows indicates the qualitative difference in the intensity of the respective energy transfers.

MTIs (formed by velocity fields with the same helicity sign) is characterized by an inverse energy cascade, while all the other combinations (where two modes have opposite helicities) lead to a forward energy cascade. Once all of them are coupled together by the whole Navier-Stokes equation we typically have a forward energy transfer, albeit a switch to an inverse cascade is observed in presence of strong rotation (Smith et al. 1996; Mininni et al. 2009) or in shallow fluid layers (Nastrom et al. 1984; Lautenschlager et al. 1988; Smith & Waleffe 1999; Celani et al. 2010; Xia et al. 2011). Concerning the full MHD case of interest here, we carried out a series of DNSs of Eqs. (9) and (10) using a fully de-aliased pseudospectral code up to 512^3 collocation points in a triply periodic domain of size $L = 2\pi$. We stir the velocity field with a random Gaussian forcing:

$$\langle \mathbf{f}_u(\mathbf{k}, t) \mathbf{f}_u^*(\mathbf{q}, t') \rangle = F_u \delta(\mathbf{k} - \mathbf{q}) \delta(t - t') \hat{Q}(\mathbf{k}),$$

where $\hat{Q}(\mathbf{k})$ is a projector assuring incompressibility and F_u is nonzero in a given band of Fourier modes (concentrated either at large or at small scales) $k_u^f \in [k_{\min} : k_{\max}]$. Moreover, by decomposing the forcing in its helical modes: $\mathbf{f}_u = \mathbf{f}_u^+ + \mathbf{f}_u^-$ we can further control the chirality of the mechanical injection. The same kind of forcing is also used for the magnetic field (when applied). Further details concerning the implementation of the helical projection can be found in (Biferale et al. 2012, 2013).

In order to test the predictions of the analysis presented in Sec. 2 and to refine the understanding of the interaction of a magnetic field in a helical flow, we carried out two sets of numerical experiments.

In the first set of simulations we studied the evolution of the magnetic field initially seeded at small-scales and without any injection of magnetic energy, i.e. only the velocity field is forced. These simulations are labeled as **linear** referring to the character of the initial magnetic growth. In this set, we studied both the case with zero or strong positive/negative initial magnetic helicity. We studied three different underlying velocity configurations: a chiral kinetic forcing at large scales, leading to a turbulent helical velocity field (**R1-D**); a chiral forcing at small scales, leading to a laminar helical velocity field (**R2-D**) and a chiral forcing at small scales combined with a strong decimation of the velocity field on only positively helical modes, leading to a turbulent helical velocity field in an inverse-cascade regime (**R3-D**). The latter case allows us to assess the growth of a small-scale magnetic field in a strongly helical turbulent flow and to select only velocity modes with the same helical sign. The label (**D**) stands for Dynamo.

The second set of simulations is denoted as **non-linear** because we add a small-scale forcing on the magnetic component also. In this second series of simulations we started from the velocity configuration (**R1-D**) described above and we investigated different sub-cases by changing the magnetic conditions: a magnetic forcing with the same sign of helicity as the mechanical forcing (**R1-IC**) and with opposite sign (**R2-IC**). The effects of a small-scale magnetic forcing is also studied starting from the decimated setup described by the class of simulations (**R3-D**), i.e. where the velocity field is constrained to evolve only on one set of helical modes. Now we inject magnetic helicity with the same or opposite sign with respect to the kinetic helicity (**R3-IC**) and (**R4-IC**) respectively. The label (**IC**) stands for Inverse (magnetic helicity) Cascade.

4.1. Large- and small-scale dynamo

In this section we report results from the numerical experiments where we let the magnetic field evolve freely in different types of flows. The initial conditions are always generated from a stationary simulation of a non-conducting fluid, and the initial magnetic seeding is always at small scales to be amplified by kinematic dynamo action. The simulations are evolved beyond the kinematic regime into the nonlinear dynamo regime. The numerical experiments discussed in this section differ in the range of scales, k_u^f , of the applied mechanical force, \mathbf{f}_u , and in the projection onto different helical sectors of the velocity field. Detailed information about this series of simulations is given in table 1.

R1-D: In this case we evolve the velocity fields with a positively helical mechanical force, $\mathbf{f}_u = \mathbf{f}_u^+$, applied at large scales, $k_u^f \in [0.25 : 1.25]$. As can be seen in Figs. 5(a-b), the growth of \mathbf{b}^+ and \mathbf{b}^- both at small and large scales is symmetric despite the helical large-scale forcing. We explain this lack of helical asymmetry in the magnetic field growth by observing that the flow is nearly mirror symmetric for $k > k_u^f$, as shown in Figs. 5(c-d). This is not surprising, it is well known that fully homogeneous and isotropic turbulence tends to quickly recover small-scale mirror symmetry even in presence of a large-scale helicity injection (Chen et al. 2003a,b; Mininni & Pouquet 2010; Sahoo & Biferale 2015; Sahoo et al. 2016; Gledzer & Chkhetiani 2015; Deusebio & Lindborg 2014; Kessar et al. 2015; Stepanov et al. 2015a,b). To quantify the rate of recovery we show in the inset of Fig. 5(d) the ratio $E_u^+(k)/(E_u^+(k) + E_u^-(k))$. As a result, unless other mechanisms, e.g. rotation or convection, enhance preferentially one small-scale helical component, the magnetic seed evolves initially on a non-helical turbulent flow and no difference is expected between the growth rate of the positively and negatively helical magnetic field components.

In case (**R2-D**) the velocity field is subjected to a small-scale helical force, $\mathbf{f}_u = \mathbf{f}_u^+$ with $k_u^f \in [32 : 40]$. With small-scale injection of kinetic energy, the forward energy cascade cannot develop and the flow is laminar. Now, from Figures 6(a-b) we observe an asymmetric growth of positively and negatively helical magnetic field consistent with the analytical predictions from the MTI systems D2 and D3 discussed in Secs. 3.1 and 3.2 and depicted in Figs. 2 and 3. The curves are always color-coded with darker colors indicating later times, with the time evolution of the magnetic energy shown in Fig. 8(a) on a linear-logarithmic scale in order to indicate when the kinematic stage of the dynamo ends and the evolution of the magnetic field becomes nonlinear. Time is expressed in units of large-scale eddy-turn-over time T (see table 1), and the color-coded arrows in Fig. 8(a) correspond to the color-coded spectra shown in Figs. 6(a-b). In figures 6(c-d) the evolution of the kinetic energy spectra is also shown. As can be seen from Figs. 6(a-b), at scales larger than the forcing scale the negatively helical modes grow faster than the positively helical modes, while the opposite is true at scales smaller than the forcing scale. This is also quantified in the inset of Fig. 6(b) where the ratio $E_b^-(k)/(E_b^+(k) + E_b^-(k))$ is plotted at different times. The above empirical observation is precisely the expected helical signature of an STF-dynamo operating in a positively helical flow as expressed by statements (i) and (ii) in Sec. 3.1 and statement (iii) in Sec. 3.2. As explained in Secs. 3.1 and 3.2 and summarized in statement (iv) in Sec. 3.2. Interestingly, the STF-type dynamo continues beyond the kinematic regime as can be seen in Figs. 6(a-d), where at later times the magnetic field is not negligible and has a clearly visible feedback on the evolution of the kinetic energy. As indicated in Fig. 8(a), the two curves representing $t/T = 2.39$ and $t/T = 3.34$ shown as dark lines in Figs. 6(a-b) correspond to snapshots of the magnetic field during nonlinear evolution, while the two earlier snapshots at $t/T = 0.16$ and $t/T = 0.32$ shown as light gray curves correspond to the kinematic stage of the dynamo. As can be seen from Figs. 6(a-b), at the largest resolved scale $E_b^-(k)$ grows better than $E_b^+(k)$, even in the nonlinear regime. However, we also observe a saturation effect and at later times the difference in the growth of positively and negatively helical sectors diminishes. At that late stage, both magnetic and kinetic energy spectra have a slope qualitatively compatible with $k^{-5/3}$ -scaling at low wavenumbers, while at intermediate wavenumbers the positively helical components $E_b^+(k)$ and $E_u^+(k)$ have a k^2 slope.

The growth of the magnetic field in the non-standard case given by the setup (**R3-D**) is shown in Figs. 7(a-b). Here the velocity field is again forced at small scales, but at difference from the case (**R2-D**) initially in an inverse-cascade regime, i.e. with fully turbulent helical modes at all scales. This is achievable due to the fact that we have constrained the Navier-Stokes velocity evolution only on positive helical modes (Biferale et al. 2012, 2013). The interest in studying this case is twofold. First, we want to understand how robust the inverse kinetic transfer is under magnetic perturbations. Second, we want to study the evolution of a small-scale magnetic field in a fully helical turbulent flow. From Figs. 7(a-b), we see that the magnetic growth is very similar to the case (**R2-D**) further confirming the theoretical triad-by-triad analysis. Interestingly, the magnetic field growth has a dramatic effect on the inverse kinetic energy cascade, as demonstrated in Fig. 7(c) where the $k^{-5/3}$ -slope of $E_u^+(k)$ is immediately destroyed. In other words, the magnetic field grows at the expense of the velocity field modes, strongly perturbing the phase-correlation leading to the inverse transfer in absence of magnetic perturbations. Eventually a k^2 -scaling for $E_u(k) = E_u^+(k)$ develops at

late times for intermediate k , as in the laminar case **R2-D**. The time evolution of the magnetic energy is shown in Fig. 8(b) on a linear-logarithmic scale, with color-coded arrows indicating that the curves at $t/T = 5.5$, $t/T = 10.44$ and $t/T = 20.88$ shown in Fig. 7 correspond to the nonlinear stage of the dynamo, while the curve at $t/T = 0.55$ shows a snapshot in the kinematic stage. Similar to case **(R2-D)**, we observe that the STF-type dynamo continues to be active in the nonlinear regime, albeit showing slower magnetic field growth and less difference between the growth of the positive and negatively helical sectors.

In summary, we find in both cases **(R2-D)** and **(R3-D)** that the linear dynamics appear to be quite strong, as the magnetic field evolution still bears the same helical signature even in the nonlinear dynamo regime. As can be expected, this effect diminishes with time as the overall magnetic field growth tends to saturate. In relation to the predictions from the linear stability analysis we conclude that the results from the triadic dynamics describe the evolution of the magnetic field well during the kinematic stage of the dynamo as well as during the onset of nonlinear evolution, even in the presence of a large number of interacting modes. Eventually the validity of the predictions breaks down due to saturation.

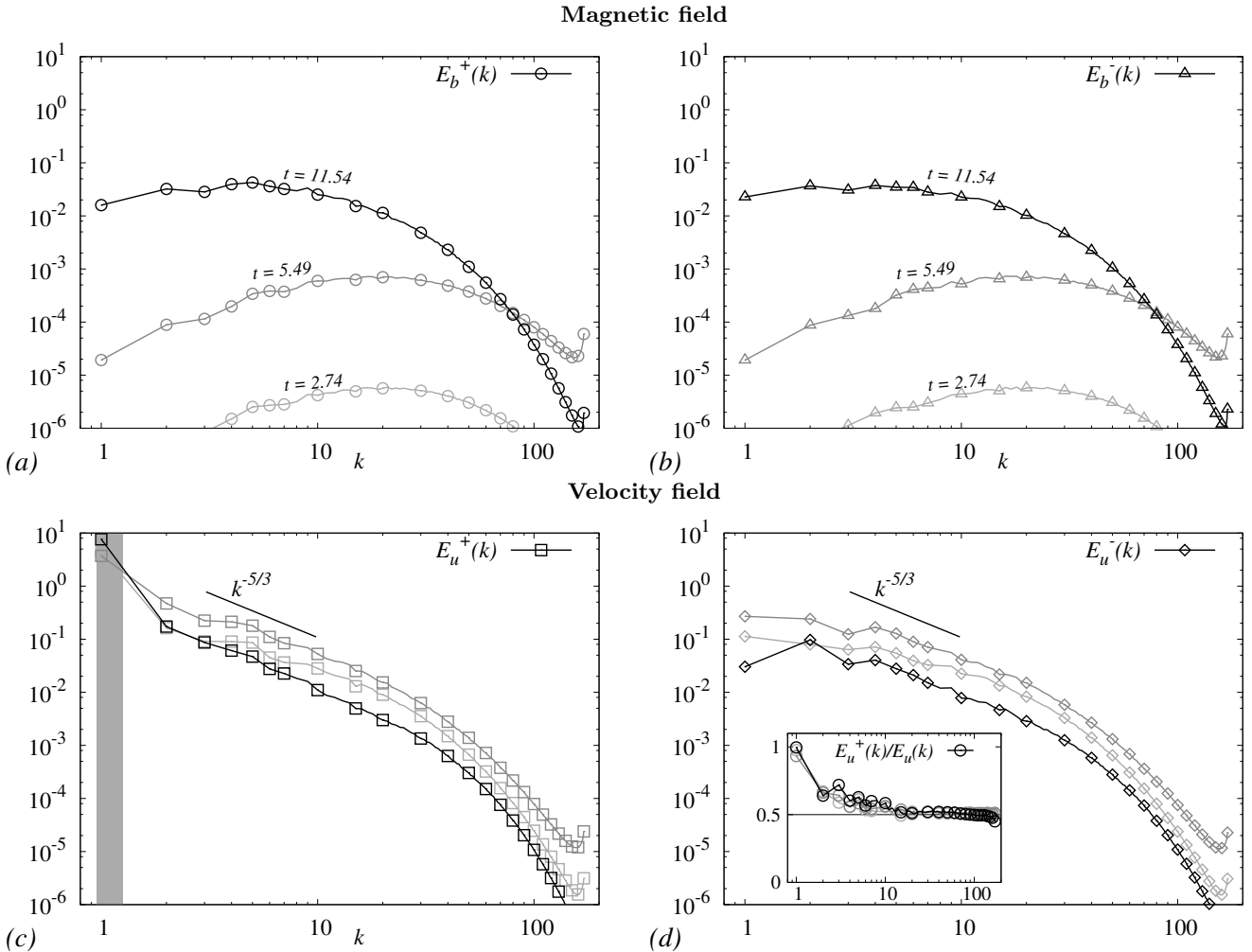


Figure 5. Run **R1-D**. Panels (a) and (b): Log-log plot of the magnetic energy spectra $E_b^+(k)$ and $E_b^-(k)$ against k at different times. Panels (c) and (d): the same as (a) and (b) but for the kinetic energy spectra $E_u^+(k)$, $E_u^-(k)$. Time is expressed in units of the large-scale eddy-turn-over time, T (see table 1). The gray color-coding corresponds to different instants during the time evolution, while the dark rectangular area corresponds to the band of forced wavenumbers. Inset of panel (d): Ratio of the kinetic energy in the positively helical modes with respect to the total kinetic energy, $E_u^+(k)/E_u(k)$; the solid horizontal line marks the value 0.5 which corresponds to the mirror symmetric case.

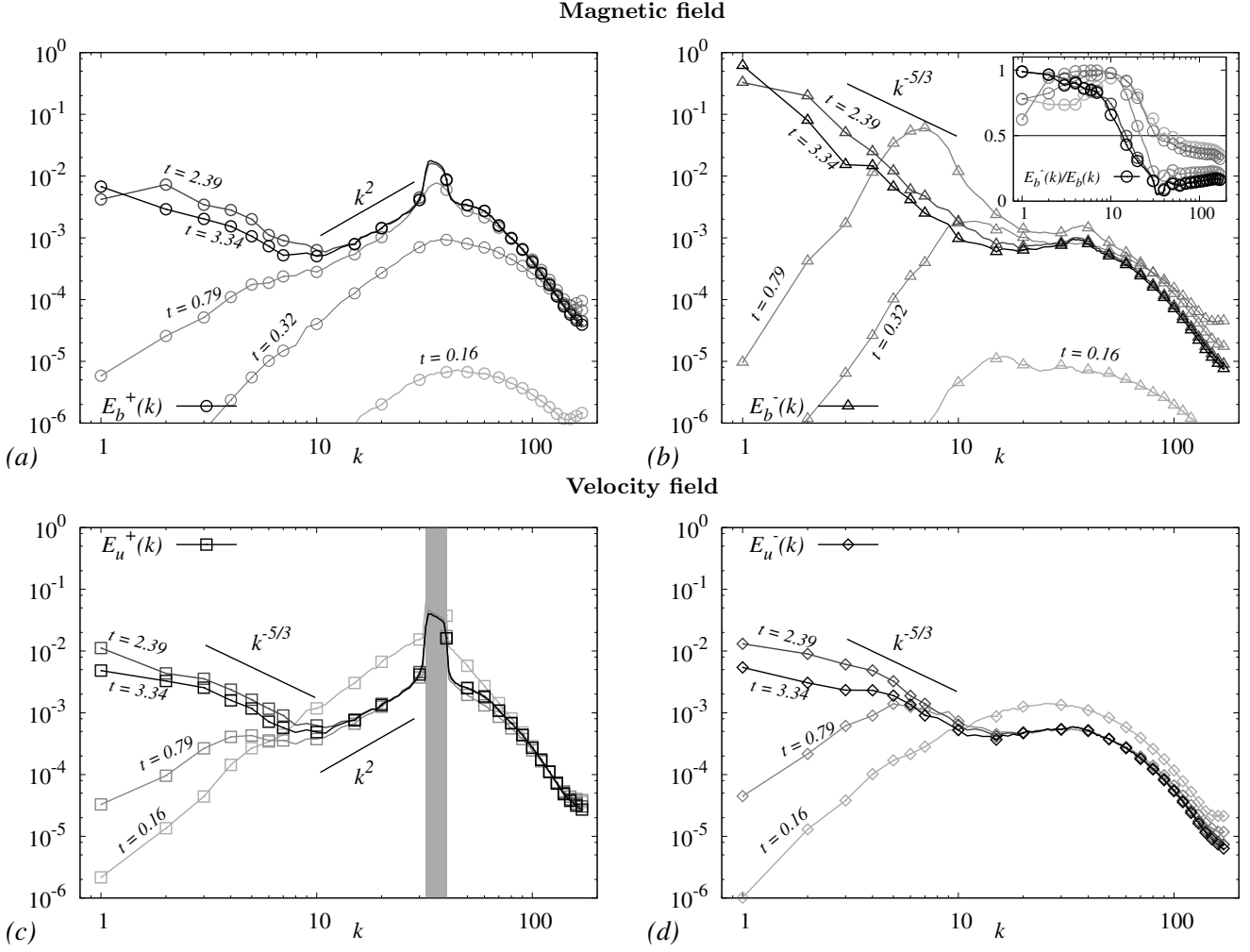


Figure 6. Run **R2-D**. Panels (a) and (b): Log-log plot of the magnetic energy spectra $E_b^+(k)$ and $E_b^-(k)$ against k at different times. Inset of panel (b): Ratio of the magnetic energy in the positively helical modes with respect to the total magnetic energy, $E_b^+(k)/E_b(k)$; the solid horizontal line marks the value 0.5 which corresponds to the mirror symmetric case. Panels (c) and (d): the same as (a) and (b) but for the kinetic energy spectra $E_u^+(k)$ and $E_u^-(k)$.

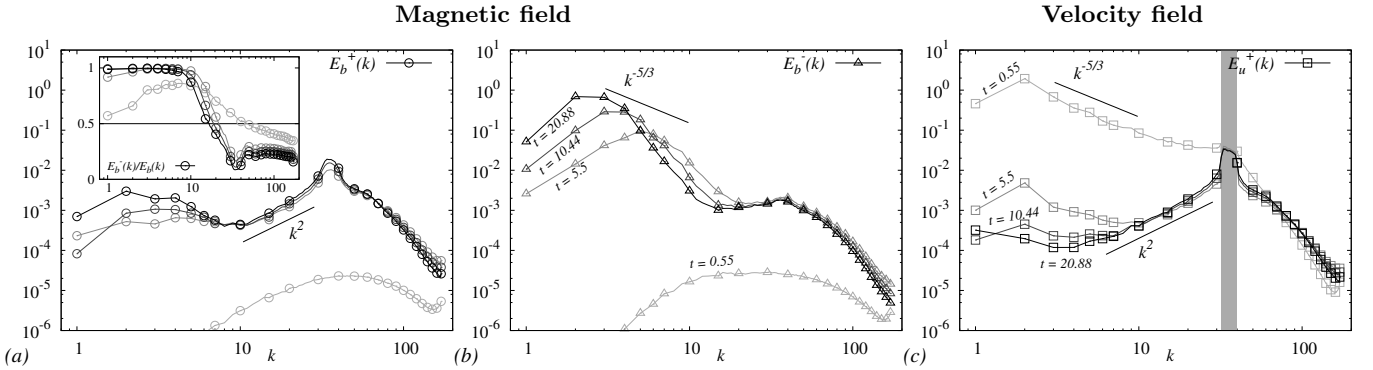


Figure 7. Run **R3-D**. Panels (a) and (b): Log-log plot of the magnetic energy spectra $E_b^+(k)$ and $E_b^-(k)$ against k at different times. Inset of panel (a): Ratio of the magnetic energy in the positively helical modes with respect to the total magnetic energy, $E_b^+(k)/E_b(k)$; the solid horizontal line marks the value 0.5 which corresponds to the mirror symmetric case. Panel (c): the same as (a) and (b) but for the kinetic energy spectrum $E_u(k) = E_u^+(k)$.

4.2. Inverse cascade of magnetic helicity

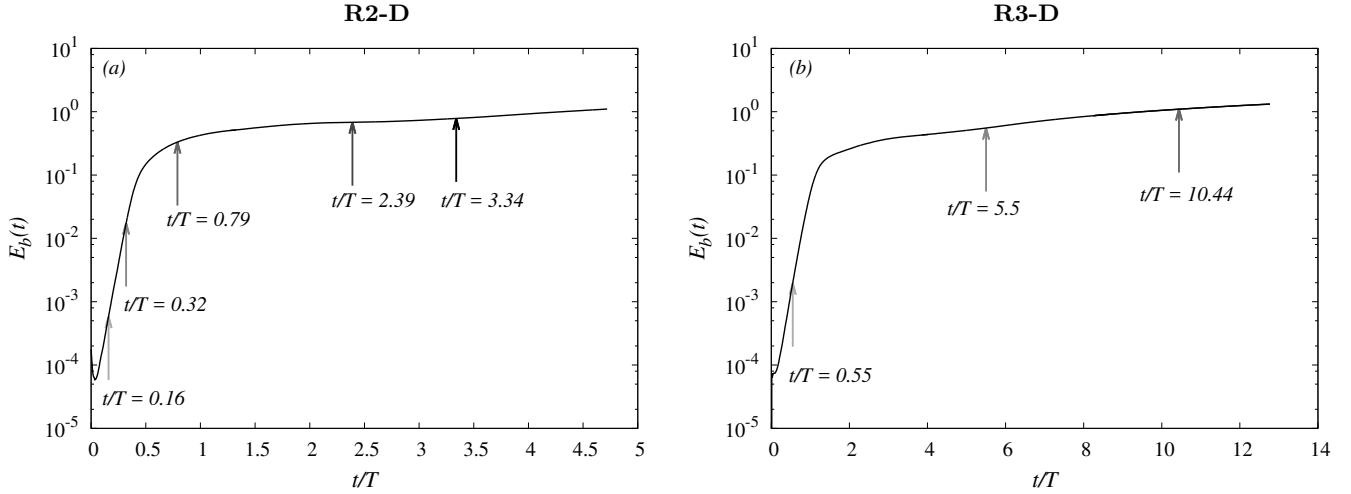


Figure 8. Time series of the total magnetic energy on a linear-logarithmic scale for runs **R2-D** (panel (a)) and **R3-D** (panel (b)). The arrows in panels (a) and (b) indicate the time corresponding to the magnetic energy spectra shown in Figs. 6(a-b) and 7(a-b), respectively. Time is given in units of large eddy turnover time T , as specified in table 1. In order to improve the readability of the figure showing clearly the initial exponential growth, the time evolution in panel (b) is only given up to $t/T = 13$.

In order to assess the dynamics of strongly magnetized flows and in particular of the inverse cascade of magnetic helicity, we carried out a series of simulations subjecting the system to small-scale electromagnetic forces with $k_b^f \in [32 : 40]$, also. Similar to the previous section, we distinguish the simulations according to the characteristic scale of the mechanical force and the helical content of the velocity field. Full details of this series of numerical experiments are contained in table 2.

4.2.1. Full velocity field

In cases **R1-IC** and **R2-IC** the force is either positively helical $\mathbf{f}_b = \mathbf{f}_b^+$, or negatively helical, $\mathbf{f}_b = \mathbf{f}_b^-$. Results for the time evolution of these two configurations are shown in Figs. 9 and 10, respectively. From a comparison of Fig. 9(a) with Fig. 10(b), it is clear that the evolution of the magnetic energy spectra is fully dominated by the signature of the magnetic forcing, i.e. there is always an inverse cascade of the same magnetic helical component injected at small scales. An important indicator for a cascade process is given by the flux of the cascading quantity. As can be seen in

Table 1. Details of the linear (dynamo) simulations. N : number of collocation points along each axis in a periodic cube of size $L = 2\pi$; ν : kinematic viscosity; η : magnetic resistivity; k_u^f : range of forced wavenumbers for velocity field; T : large-eddy turnover time (L/u_{rms}); ε : kinetic dissipation rate; Re_λ : Taylor-scale Reynolds number.

RUN	N	helical modes	$\nu = \eta$	k_u^f	f_u^+	f_u^-	T	ε	Re_λ	
R1-D	512	$\mathbf{u}^+, \mathbf{u}^-, \mathbf{b}^+, \mathbf{b}^-$	0.002	[0.25, 1.25]	5	0	1.82	2.5	230	nonhelical dynamo, turbulent flow
R2-D	512	$\mathbf{u}^+, \mathbf{u}^-, \mathbf{b}^+, \mathbf{b}^-$	0.002	[32, 40]	5	0	6.28	3.5	15	large-scale dynamo, laminar flow
R3-D	512	$\mathbf{u}^+, \mathbf{b}^+, \mathbf{b}^-$	0.002	[32, 40]	5	–	1.82	6.2	140	helical dynamo, turbulent flow

Table 2. Details of the non-linear (inverse cascade) simulations. N : number of collocation points along each axis in a periodic cube of size $L = 2\pi$; ν : kinematic viscosity; η : magnetic resistivity; k_u^f : range of forced wavenumbers for velocity field; k_b^f : range of forced wavenumbers for magnetic field; $T = L/u_{\text{rms}}$: large-eddy turnover time; ε : kinetic dissipation rate; Re_λ : Taylor-scale Reynolds number.

RUN	N	helical modes	$\nu = \eta$	k_u^f	k_b^f	f_u^+	f_u^-	f_b^+	f_b^-	T	ε	Re_λ
R1-IC	512	$\mathbf{u}^+, \mathbf{u}^-, \mathbf{b}^+, \mathbf{b}^-$	0.002	[0.25, 1.25]	[32, 40]	1	0	25	0	1.82	2.5	230
R2-IC	512	$\mathbf{u}^+, \mathbf{u}^-, \mathbf{b}^+, \mathbf{b}^-$	0.002	[0.25, 1.25]	[32, 40]	1	0	0	25	1.82	2.5	230
R3-IC	512	$\mathbf{u}^+, \mathbf{b}^+, \mathbf{b}^-$	0.002	[32, 40]	[32, 40]	5	–	25	0	1.82	6.2	140
R4-IC	512	$\mathbf{u}^+, \mathbf{b}^+, \mathbf{b}^-$	0.002	[32, 40]	[32, 40]	5	–	0	25	1.82	6.2	140

the inset of Fig. 9(b), the magnetic helicity flux

$$\Pi_{H_m}(k) = \sum_{k_{min}}^k \sum_{|\mathbf{k}'=k'} \mathbf{b}_{\mathbf{k}'}^* \cdot i\mathbf{k} \times \sum_{\mathbf{k}+\mathbf{p}+\mathbf{q}=0} \mathbf{u}_{\mathbf{p}} \times \mathbf{b}_{\mathbf{q}} + \text{c.c.}, \quad (48)$$

is constant and positive in the region $1 < k < k_b^f$, indicating indeed an inverse *cascade* of positive magnetic helicity. At difference from the dynamo case, the large-scale magnetic helicity has the same signature of the small-scale kinetic helicity. This is possible because of the strong intensity of the small-scale magnetic field which is always far from a kinematic dynamo regime. This is in agreement with statement (v) of the theoretical section 3.3. Comparing Fig. 9(c) with Fig. 10(d) it is important to notice that the feedback of the magnetic field via the Lorentz force on the velocity field leaves a small-scale helical signature on the flow itself. This is quantified in the insets of Figs. 9(d) and 10(d). On the other hand, the magnetic feedback on the large-scale velocity field tends to make it helically neutral, recovering large-scale mirror symmetry as shown in the insets of Figs. 9(d) and 10(d).

In summary, we find that the injection of magnetic helicity leads to large-scale magnetic field growth mainly of the forced helical sector of the magnetic field, as expected from the inverse cascade of magnetic helicity and consistent with the theoretical results summarized in statement (v) of Sec. 3.3. We also find that the conversion of magnetic to kinetic energy due to the action of the Lorentz force at small-scales proceeds preferentially between magnetic and velocity field modes with the same sign of helicity.

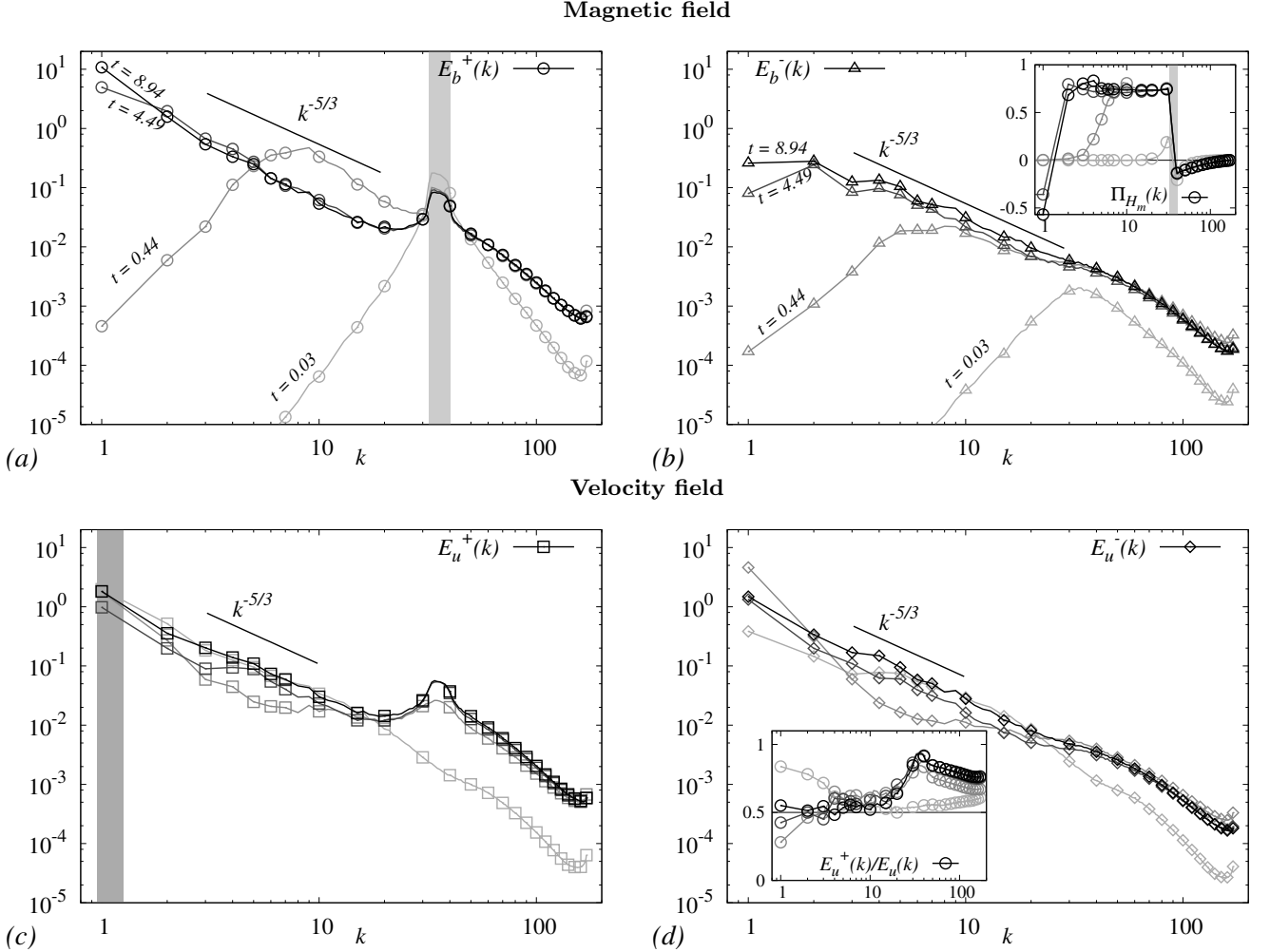


Figure 9. Run R1-IC. Panels (a) and (b): Log-log plot of the magnetic energy spectra $E_b^+(k)$ and $E_b^-(k)$ against k at different times. Inset of panel (b): Flux of magnetic helicity $\Pi_{H_m}(k)$. Panels (c) and (d): the same as (a) and (b) but for the kinetic energy spectra $E_u^+(k)$ and $E_u^-(k)$. Inset of panel (d): Ratio of the kinetic energy in the positively helical modes with respect to the total kinetic energy, $E_u^+(k)/E_u^-(k)$; the solid horizontal line marks the value 0.5 which corresponds to the mirror symmetric case.

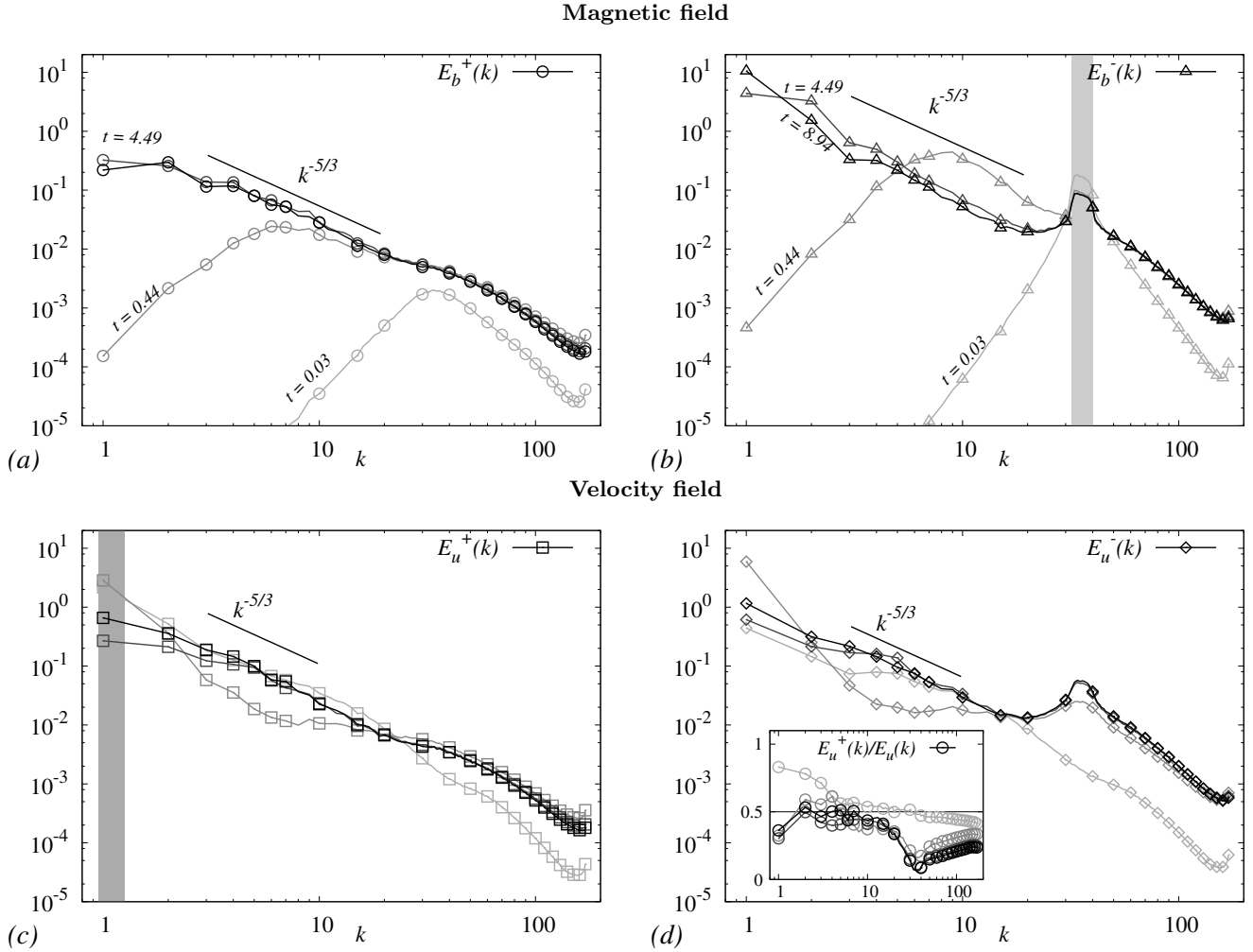


Figure 10. Run **R2-IC**. Panels (a) and (b): Log-log plot of the magnetic energy spectra $E_b^+(k)$ and $E_b^-(k)$ against k at different times. Panels (c) and (d): the same as (a) and (b) but for the kinetic energy spectra $E_u^+(k)$ and $E_u^-(k)$. Inset of panel (d): Ratio of the kinetic energy in the positively helical modes with respect to the total kinetic energy, $E_u^+(k)/E_u(k)$; the solid horizontal line marks the value 0.5 which corresponds to the mirror symmetric case.

4.2.2. Decimated helical velocity field

We now focus on the evolution of a strong magnetic field in a flow where the velocity is constrained to have only positive helical modes, such that we expect to see differences in the evolution of positively and negatively helical magnetic modes due to the asymmetry of the advecting flow. Again we consider two cases which only differ in the helical content of the electromagnetic force, which allows us to examine the effect of kinetic helicity on the dynamics of the inverse magnetic helicity cascade. In case **R3-IC** the base flow, $\mathbf{u} = \mathbf{u}^+$, and the electromagnetic force $\mathbf{f}_b = \mathbf{f}_b^+$, have the same sign of helicity, while in case **R4-IC** the force $\mathbf{f}_b = \mathbf{f}_b^-$ is of opposite helicity compared to the flow. The time evolution of the helical magnetic energy spectra is shown in Fig. 11(a-b) for case **R3-IC** and in Fig. 12(a-b) for case **R4-IC**. We observe a pronounced large-scale magnetic field growth in the forced helical sector in both cases, as expected from the theoretical results on linear instabilities of the triadic dynamics summarized by statement (v) in Sec. 3.3. The large-scale growth of $E_b^+(k)$ in case **R3-IC** and $E_b^-(k)$ in case **R4-IC** are associated with the inverse cascade of magnetic helicity. Visualisations of the magnitude of the full magnetic field \mathbf{b} and of the helical components \mathbf{b}^+ and \mathbf{b}^- for case **R3-IC** are shown in Fig. 13, where the formation of large-scale positively helical structures is clearly visible. The visualised data has been filtered with a sharp Fourier filter keeping only modes at wavevectors \mathbf{k} with $|\mathbf{k}| \leq 20$ in order to remove the small-scale contribution from the forcing. Nevertheless, the inverse cascade is more efficient for **R3-IC** compared to **R4-IC**. Indeed as can be seen from Fig. 11(a), $E_b^+(k)$ grows more efficiently than $E_b^-(k)$ in Fig. 12(b). This confirms the prediction from the stability analysis concerning the inverse cascade of magnetic helicity summarized in statement (vi) in Sec. 3.3. This shows that the kinetic helicity has a profound

effect on the efficiency of nonlinear interactions distributing magnetic helicity across the scales: *The inverse cascade of magnetic helicity in a helical flow is more efficient and more nonlocal if kinetic and magnetic helicity are of the same sign.*

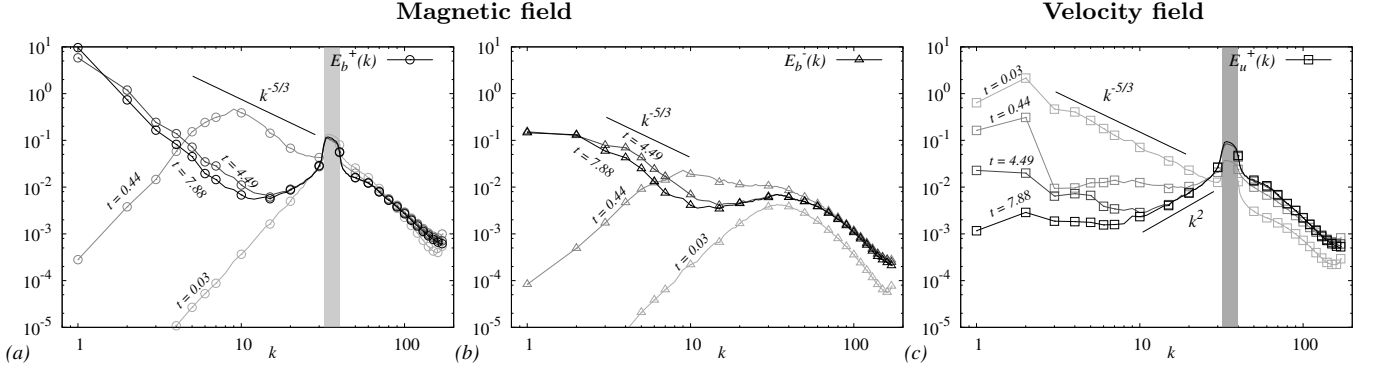


Figure 11. Run **R3-IC**. Panels (a) and (b): Log-log plot of the magnetic energy spectra $E_b^+(k)$ and $E_b^-(k)$ against k at different times. Panel (c): the same as (a) and (b) but for the kinetic energy spectrum $E_u(k) = E_u^+(k)$.

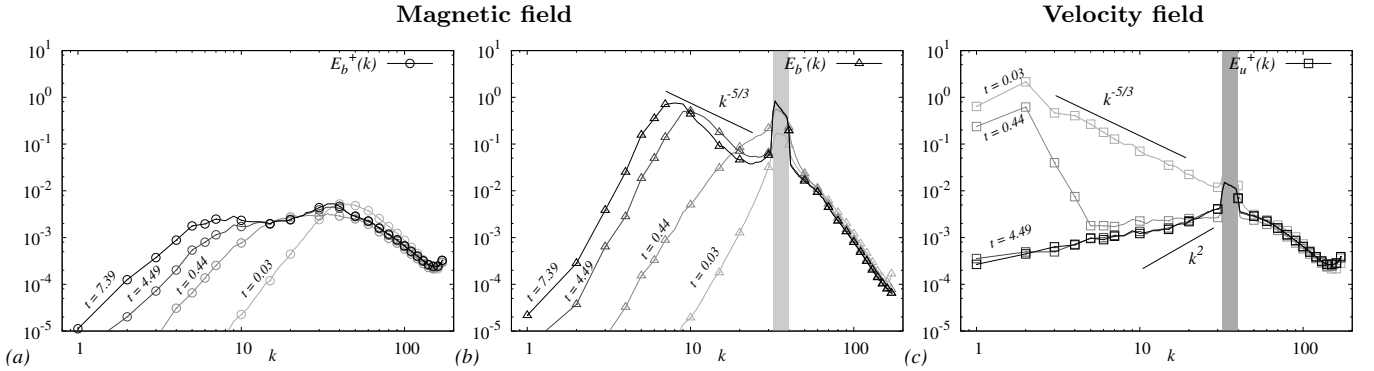


Figure 12. Run **R4-IC**. Panels (a) and (b): Log-log plot of the magnetic energy spectra $E_b^+(k)$ and $E_b^-(k)$ against k at different times. Panel (c): the same as (a) and (b) but for the kinetic energy spectrum $E_u(k) = E_u^+(k)$.

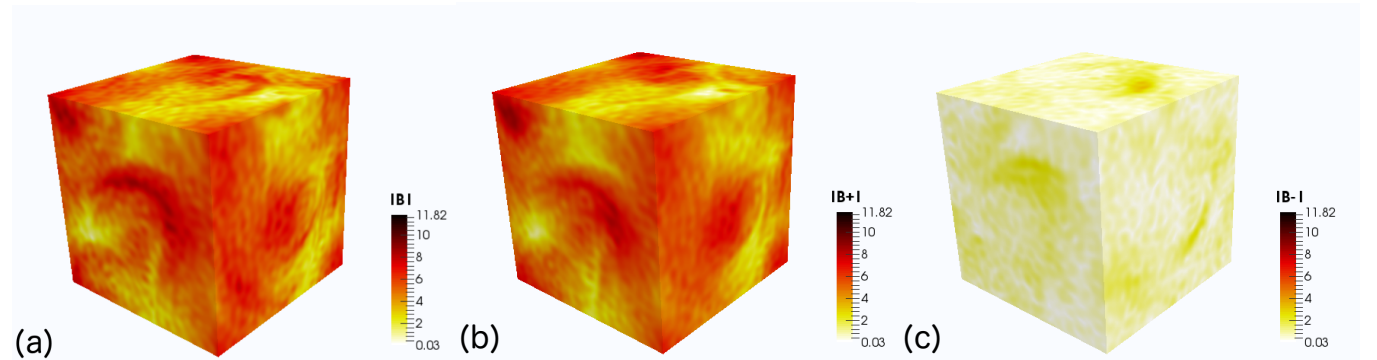


Figure 13. Visualisations of the magnetic field magnitude for run **R3-IC** at $t/T = 7.88$, which corresponds to the latest snapshot in time shown in Fig. 11. Panel (a) shows the magnitude of the full magnetic field $|\mathbf{b}|$, panel (b) shows the positively helical component $|\mathbf{b}^+|$ and panel (c) the negatively helical component $|\mathbf{b}^-|$. A sharp Fourier filter has been applied to all fields keeping only modes at wavevectors \mathbf{k} with $|\mathbf{k}| \leq 20$ in order to remove the small-scale contribution from the forcing.

5. CONCLUSIONS

We studied the dynamics of helical triad interactions in homogeneous MHD turbulence both analytically and numerically. We have shown that the helical-Fourier decomposition of the full MHD equations is a key tool to better disentangle different inertial transfer processes in the fully coupled dynamics. First, we extended the set of helical triad interactions (Lessinnes et al. 2009; Linkmann et al. 2016) to the most general MTI systems, and we clarified in which cases the stability analysis of the subset of triadic interactions carried out in (Linkmann et al. 2016) is sufficient to capture all possible linear instabilities. We further analysed two cases of astrophysical interest concerning the emergence of large scale magnetic fields, i.e. dynamo action and the inverse cascade of magnetic helicity, by extending the results presented in (Linkmann et al. 2016) to provide qualitatively testable predictions on the helical contents of the resulting magnetic growth at large- and small-scales. Subsequently we carried out two series of suitably designed numerical experiments in order to test the theoretical results. In Secs. 3.1 and 3.2 we clarified which of the linear instabilities identified in (Linkmann et al. 2016) is the leading one and which global helical signature should be expected for the magnetic field. In Sec. 3.3 we focused on linear instabilities which can be associated with the inverse cascade of magnetic helicity: *A helical magnetic equilibrium at a given scale can only be unstable with respect to like-signed helical magnetic perturbations at larger scales* (Linkmann et al. 2016). We found that the level of kinetic helicity affects the growth rates associated with the inverse magnetic helicity cascade: *The inverse cascade of magnetic helicity is more efficient in a helical flow where magnetic and kinetic helicity are of the same sign*. We point out that the perturbation problem considered for strongly magnetised flows was restricted to large-scale magnetic perturbations only, and it did not include the effect of the Lorentz force on the flow. In principle, these two dynamical effects are intimately related. A more refined analysis which distinguishes for example between nonlinear dynamo and inverse cascade effects thus requires a simultaneous analysis of the Lorentz force, which in turn requires a distinction between homo- and heterochiral MTI systems. Similarly, the possible influence of the characteristic scale of the flow on the local or non-local nature of the inverse cascade would also require a study of the general MTI system. Due to the structure of the chosen equilibria our analysis did not consider the effect of non-negligible cross-helicity on the evolution of the magnetic field. Let us remark, that the effects induced by an equilibrium solution with a non-trivial cross-helicity can also be handled analytically as shown in (Linkmann et al. 2016).

All theoretical results have been derived from a linear stability analysis of the basic triadic structure of the MHD equations where only three modes interact. However, in any physical MHD configuration all modes interact, therefore it is not immediately obvious if the theoretical results obtained from the single MTI systems correctly predict the behavior of the full dynamics (Moffatt 2014). Therefore we carried out two series of numerical experiments, where series **D** discussed in Sec. 4.1 corresponds to dynamo simulations and series **IC** in Sec. 4.2 to simulations with an inverse magnetic helicity cascade. The numerical results confirm the theoretical predictions presented in the previous paragraph.

It is important to note that the triadic dynamo instabilities analyzed here do not result from any further modeling assumptions such as scale separation or the first-order smoothing approximation (Moffatt 1978; Krause & Rädler 1980; Brandenburg & Subramanian 2005). Instead, they are present in the basic dynamics of the MHD equations restricted to a small number of degrees of freedom. Furthermore, the triadic α -type dynamo instabilities found here may not have the same limitations as the classical α -effect of mean-field electrodynamics which originate from the more efficient growth of the small-scale magnetic field compared to the large-scale magnetic field (Vainshtein & Cattaneo 1992). In the latter case, one considers the mean-field induction equation of the α -dynamo $\partial_t \mathbf{B}_0 = \alpha \nabla \times \mathbf{B}_0$, where the magnetic field \mathbf{B} has been decomposed into a large-scale mean and a small-scale fluctuating part $\mathbf{B} = \mathbf{B}_0 + \mathbf{b}$, and the coefficient α is given by $\alpha = \frac{1}{3} \left(- \langle \mathbf{u} \cdot \boldsymbol{\omega} \rangle + \langle \mathbf{b} \cdot \mathbf{j} \rangle \right)$, with the angled brackets denoting an appropriate average (Brandenburg & Subramanian 2005) and $\mathbf{j} = \nabla \times \mathbf{b}$ the current density. If the growing small-scale magnetic field \mathbf{b} and the small-scale flow \mathbf{u} have like-signed helicities, then the coefficient α decreases, thus quenching the growth rate of the large-scale magnetic field \mathbf{B}_0 . Due to the faster evolution of the small-scale magnetic field \mathbf{b} compared to the large-scale magnetic field \mathbf{B}_0 , the coefficient α could be quenched before leading to large-scale magnetic field growth. Therefore concerns have been raised in the literature about whether the classical α -effect is efficient enough to generate large-scale magnetic fields. This is especially problematic at high magnetic Reynolds numbers, eventually leading to catastrophic α -quenching (Cattaneo & Hughes 1996). Our analysis is concerned with instabilities of the ideal MHD equations, and the corresponding growth rates do not depend on the magnetic Reynolds number Rm . Hence the dynamo instabilities we found are in principle present even at large Rm . A process similar to α -quenching and/or saturation can also be studied within our approach, but it may not be catastrophic due to the independence of the growth rates on Rm . The small-scale instabilities we found in Sec. 3.2 preferentially lead to a growing small-scale

magnetic field with the same sign of helicity as the flow. Eventually the small-scale magnetic field will back-react on the flow, and the linear instability leading to the α -like large-scale dynamo may be removed. At this point we cannot be more precise, as a rigorous assessment of dynamo quenching is outside the scope of the stability analysis carried out here as it requires mixed equilibria, while only purely mechanical or electromagnetic equilibria were analyzed here. However, we point out that dynamo quenching and the effect of the Lorentz force can also be assessed by a similar kind of stability analysis. This analysis, which requires a different set of equilibria and is technically more complex, is currently in progress and will be reported elsewhere.

The α -effect has further limitations due to its intrinsic scale separation. [Boldyrev et al. \(2005\)](#) showed by considering the Kazantsev model ([Kazantsev 1968](#)) that fast-growing eigenmodes exist at all scales, which are not included in the α -dynamo due to the required scale separation. Although the Kazantsev model assumes the velocity field to have Gaussian statistics and is as such is not applicable to turbulence, the important point is that a correct description of dynamo action should involve all scales. We point out that scale separation is not necessary for the derivation of the triad-by-triad dynamo instabilities. Nevertheless, information about local and non-local dynamics can be obtained by varying the shape of the wavevector triad, and we find that strongly nonlocal triads lead mostly to α -type dynamo action.

Beyond the confirmation of the theoretical results further interesting observations can be made from the numerical work. First, the instability of a mechanical helical equilibrium associated with large-scale kinematic dynamo action appears to persist in the nonlinear regime as shown in Figs. 6 and 7 in Sec. 4.1. This suggests that a very strong magnetic field is necessary in order to quench the dynamo. Second, as shown in Figs. 9(c) and 10(d) in Sec. 4.2, the transfer of magnetic to kinetic energy due to the feedback of the Lorentz force on the flow at the small scales is sensitive to the sign of magnetic helicity: The velocity field modes with the same sign of helicity as the magnetic field increase in intensity. On the theoretical side, we found an important difference between the large-scale magnetic field growth due to dynamo instabilities compared to instabilities of the inverse cascade type, which occur due to nonlinear self-interaction in strongly magnetized flows. Dynamo action produced large-scale magnetic fields of opposite helicity compared to the small-scale flow while the inverse cascade of magnetic helicity was most efficient in the helical magnetic field sector with the same sign of helicity as the flow. This may lead to transitional behavior with increasing small-scale magnetic field strength, eventually changing the helical signature of the large-scale magnetic field. Furthermore, it suggests the possible existence of a dynamo quenching mechanism at the basic triad level.

ACKNOWLEDGEMENTS

We thank V. Dallas for helpful discussions. The research leading to these results has received funding from the European Union's Seventh Framework Programme (FP7/2007-2013) under grant agreement No. 339032. ML acknowledges support from the Scottish Universities Physics Alliance and the UK Engineering and Physical Sciences Research Council (EP/K503034/1). The theoretical work was planned and carried out by ML, GS designed and carried out all numerical simulations and performed the data analysis. LB contributed to the theoretical work and designed the numerical simulations. Everyone contributed to the interpretation of the numerical results. The paper was written by ML and LB.

APPENDIX

A. COUPLING COEFFICIENTS

The results in Secs. 3.1-3.3 were derived by analyzing the structure of the coupling factors g^{IN} , g^{LF} , g^{M1} and g^{M2} , which quantify the strength and locality of a given combination of helical modes. We begin by stating the definition of a generic coupling factor associated to a given triadic interaction

$$g_{s_k s_p s_q}^X = -\frac{1}{2} \mathbf{h}_k^{s_k*} \cdot \left(\mathbf{h}_p^{s_p*} \times \mathbf{h}_q^{s_q*} \right) = s_k s_p s_q e^{-i\beta} \frac{Q}{4kpq} (s_k k + s_p p + s_q q), \quad (\text{A1})$$

where $Q^2 = 2(k^2 p^2 + p^2 q^2 + q^2 k^2) - k^4 - p^4 - q^4 \geq 0$ depends on the shape of the triad and $\beta = \beta(s_k, s_p, s_q, k, p, q)$ is a real number determined by the orientation of the triad ([Waleffe 1992](#)) and the superscript X stands for any of the identifiers IN , LF , $M1$ and $M2$. As can be seen, the coupling factor only depends on the geometry of the wavevector triad and not on the type of interaction. This immediately implies that the product of the coupling factors which

appear in the second-order evolution equations of the perturbations of a helical mechanical or magnetic equilibrium in Sec. 3 are always positive, as only combinations with the same helical content occur

$$\begin{aligned} g_{s_k s_p s_q}^{X1} g_{s_k s_p s_q}^{X2*} &= \left(s_k s_p s_q e^{-i\beta} \frac{Q}{4k p q} (s_k k + s_p p + s_q q) \right) \left(s_q s_k s_p e^{-i\beta} \frac{Q}{4k p q} (s_q q + s_k k + s_p p) \right)^* \\ &= \left(\frac{Q}{4k p q} \right)^2 (s_k k + s_p p + s_q q)^2 = |g_{s_k s_p s_q}^{X1}|^2 = |g_{s_k s_p s_q}^{X2}|^2, \end{aligned} \quad (\text{A2})$$

where $X1$ and $X2$ label the different interactions, and we note that an inertial coupling factor g^{IN} never couples to any of the others. Equation (A2) holds for any permutation of s_k , s_p and s_q . That is, the product of two coupling factors in a given interaction always equals the modulus square of one of the factors. The second step in the analysis required an ordering of the product of coupling factors. Since the term $(Q/4k p q)^2$ in eq. (A2) is independent of the combination of helical modes, the relative ordering of the coupling coefficients is determined by the term $(s_k k + s_p p + s_q q)^2$ in eq. (A2), i.e. it depends on the helicities and the ordering of wavenumbers in a given triad. In this paper we chose without loss of generality the wavenumber ordering $k \leq q \leq p$ and obtain

$$(k + p + q)^2 \geq (-k + p + q)^2 \geq (k + p - q)^2 \geq (k - p + q)^2, \quad (\text{A3})$$

which results in

$$|g_{++++}^X| \geq |g_{-+++}^X| \geq |g_{+--+}^X| \geq |g_{+--+}^X|, \quad (\text{A4})$$

where the subscripts in this equation correspond to the different possible helicity combinations for $g_{s_k s_p s_q}^X$, that is, s_k is always the left subscript, s_p the middle subscript and s_q the right subscript. The ordering is invariant under reflections, i.e. the same ordering holds if $+$ and $-$ are interchanged. Finally, for the two large-scale dynamo classes D2 and D3 we obtain for the ratio of the prefactors in eqs. (26) and (27)

$$\frac{g_{+-+}^{M1} g_{+++}^{M2*}}{g_{-++}^{M1} g_{+++}^{M2*}} = \frac{|g_{+-+}^{M1}|^2}{|g_{-++}^{M1}|^2} = \frac{|k + p_0 - q|^2}{|-k + p_0 + q|^2} < 1. \quad (\text{A5})$$

Similarly, for the small-scale dynamo we obtain for the ratio of the prefactors in eqs. (35) and (36)

$$\frac{g_{+-+}^{M1} g_{+++}^{M2*}}{g_{-++}^{M1} g_{+++}^{M2*}} = \frac{|g_{+-+}^{M1}|^2}{|g_{-++}^{M1}|^2} = \frac{|k_0 + p - q|^2}{|k_0 - p + q|^2} > 1. \quad (\text{A6})$$

Finally, for the ratio of the prefactors in the inverse cascade processes in eqs. (43) and (44) we obtain

$$\frac{g_{++++}^{M1} g_{++++}^{LF*}}{g_{++++}^{M1} g_{++++}^{LF*}} = \frac{|g_{++++}^{M1}|^2}{|g_{++++}^{M1}|^2} = \frac{|k + p_0 + q|^2}{|k + p_0 - q|^2} > 1. \quad (\text{A7})$$

REFERENCES

- Alexakis, A. 2016, arxiv:1606.02540
 Alexakis, A., Mininni, P. D., & Pouquet, A. 2006, *ApJ*, 640, 335
 Balsara, D., & Pouquet, A. 1999, *Phys. Plasmas*, 6, 89
 Belenkaya, E. S. 2009, *Physics-Usppekhi*, 52, 765
 Biferale, L., Musacchio, S., & Toschi, F. 2012, *Phys. Rev. Lett.*, 108, 164501
 —. 2013, *J. Fluid Mech.*, 730, 309
 Biferale, L., & Titi, E. S. 2013, *Journ. Stat. Phys.*, 151, 1089
 Biskamp, D. 1993, *Nonlinear Magnetohydrodynamics.*, 1st edn. (Cambridge University Press)
 —. 2003, *Magnetohydrodynamic Turbulence.*, 1st edn. (Cambridge University Press)
 Boldyrev, S. 2005a, *ApJ*, 626, L37
 —. 2005b, *Phys. Rev. Lett.*, 96, 115002
 Boldyrev, S., Cattaneo, F., & Rosner, R. 2005, *Phys. Rev. Lett.*, 95, 255001
 Brandenburg, A. 2001, *ApJ*, 550, 824
 Brandenburg, A. 2003, in *Turbulence and Magnetic Fields in Astrophysics*, Lecture Notes in Physics 614, ed. E. Falgarone & T. Passot (Springer, Berlin Heidelberg), 402–413
 Brandenburg, A., & Subramanian, K. 2005, *Physics Reports*, 417, 1
 Cattaneo, F., & Hughes, D. W. 1996, *Phys. Rev. E*, 54, R4532
 Celani, A., Musacchio, S., & Vincenzi, D. 2010, *Phys. Rev. Lett.*, 104, 184506
 Chen, Q., Chen, S., & Eyink, G. L. 2003a, *Phys. Fluids*, 15, 361
 Chen, Q., Chen, S., Eyink, G. L., & Holm, D. D. 2003b, *Phys. Rev. Lett.*, 90, 214503
 Childress, S., & Gilbert, A. D. 1995, *Stretch, Twist, Fold: The Fast Dynamo* (Springer, Berlin)
 Cho, J. 2011, *Phys. Rev. Lett.*, 106, 191104
 Constantin, P., & Majda, A. 1988, *Commun. Math. Phys.*, 115, 435
 De Pietro, M., Biferale, L., & Mailybaev, A. A. 2015, *Phys. Rev. E*, 92, 043021
 Deusebio, E., & Lindborg, E. 2014, *J. Fluid Mech.*, 755, 654
 Dobrowolny, M., Mangeney, A., & Veltri, P. 1980, *Phys. Rev. Lett.*, 45, 144
 Frick, P., Noskov, V., Denisov, S., & Stepanov, R. 2010, *Phys. Rev. Lett.*, 105, 184502

- Frisch, U. 1995, *Turbulence: The Legacy of Kolmogorov* (Cambridge University Press)
- Frisch, U., Pouquet, A., Léorat, J., & Mazure, A. 1975, *J. Fluid Mech.*, 68, 769
- Gailitis, A., Lielausis, O., Dement'ev, S., et al. 2000, *Phys. Rev. Lett.*, 84, 4365
- Gailitis, A., Lielausis, O., Platacis, E., et al. 2001, *Phys. Rev. Lett.*, 86, 3024
- Galtier, S., & Bhattacharjee, A. 2003, *Phys. Plasmas*, 10, 3065
- . 2005, *Plasmas Phys. Control Fusion*, 47, B691
- Galtier, S., & Meyrand, R. 2014, *J. Plasma Phys.*, 81, 325810106
- Gledzer, E. B., & Chkhetiani, O. G. 2015, *ETP Letters*, 102, 465
- Goldreich, P., & Sridhar, S. 1995, *Astrophys. J.*, 438, 763
- Goodman, J., & Ji, H. 2002, *J. Fluid Mech.*, 462, 395
- Iroshnikov, P. S. 1964, *Soviet Astronomy*, 7, 566
- Kazantsev, A. P. 1968, *Sov. Phys. JETP*, 26, 1031
- Kessar, M., Plunian, F., Stepanov, R., & Balarac, G. 2015, *Phys. Rev. E*, 92, 031004(R)
- Kraichnan, R. H. 1965, *Phys. Fluids*, 8, 1385
- . 1967, *Phys. Fluids*, 10, 1417
- Krause, F., & Rädler, K. 1980, *Mean-Field Magnetohydrodynamics and Dynamo Theory* (Pergamon Press, Ltd., Oxford)
- Lautenschlager, M., Eppel, D. P., & Thacker, W. C. 1988, *Beitr. Phys. Atmosph.*, 61, 87
- Lessinnes, T., Plunian, F., & Carati, D. 2009, *Theor. Comput. Fluid Dyn.*, 23, 439
- Lessinnes, T., Plunian, F., Stepanov, R., & Carati, D. 2011, *Phys. Fluids*, 23, 035108
- Linkmann, M. F., Berera, A., McKay, M. E., & Jäger, J. 2016, *J. Fluid Mech.*, 791, 61
- Malapaka, S. K., & Müller, W.-C. 2013, *Astrophys. Journal*, 778
- Matthaeus, W. H., & Zhou, Y. 1989, *Phys. Fluids B*, 1, 1929
- Mininni, P. D. 2011, *Annu. Rev. Fluid Mech.*, 43, 377
- Mininni, P. D., Alexakis, A., & Pouquet, A. G. 2009, *Phys. Fluids*, 21, 015108
- Mininni, P. D., & Pouquet, A. G. 2010, *Phys. Fluids*, 22, 035105
- Moffatt, H. K. 1969, *J. Fluid Mech.*, 35, 117
- . 1978, *Magnetic Field Generation in Electrically Conducting Fluids* (Cambridge University Press)
- . 2014, *J. Fluid Mech.*, 741, R3
- Müller, W. C., Malapaka, S. K., & Busse, A. 2012, *Phys. Rev. E*, 85, 015302
- Nastrom, G. D., Gage, K. S., & Jasperson, W. H. 1984, *Nature*, 310, 36
- Nornberg, M. D., Spence, E. J., Kendrick, R. D., Jacobson, C. M., & Forest, C. B. 2006, *Phys. Plasmas*, 13, 055901
- Plihon, N., Boussetin, G., Palermo, F., et al. 2014, *J. Plasma Physics*, 81, 345810102
- Pope, S. B. 2000, *Turbulent Flows* (Cambridge University Press)
- Pouquet, A., Frisch, U., & Léorat, J. 1976, *J. Fluid Mech.*, 77, 321
- Priest, E. 2014, *Magnetohydrodynamics of the Sun* (Cambridge University Press)
- Priest, E., & Forbes, T. 2000, *Magnetic Reconnection: MHD theory and applications* (Cambridge University Press)
- Sahoo, G., & Biferale, L. 2015, *Eur. Phys. J. E*, 38, 1
- Sahoo, G., Bonaccorso, F., & Biferale, L. 2015, *Phys. Rev. E*, 92, 051002
- Sahoo, G., DePietro, M., & Biferale, L. 2016, arXiv:1607.05518
- Smith, L. M., Chasnov, J. R., & Waleffe, F. 1996, *Phys. Rev. Lett.*, 77, 2467
- Smith, L. M., & Waleffe, F. 1999, *Phys. Fluids*, 11, 1608
- Steenbeck, M., Krause, F., & Rädler, K.-H. 1966, *Z. Naturforsch. A*, 21, 369
- Stepanov, R., Frick, P., & Mizeva, I. 2015a, *Astrophys. J.*, 798, L35
- Stepanov, R., Golbraikh, E., Frick, P., & Shestakov, A. 2015b, *Phys. Rev. Lett.*, 115, 234501
- Stieglitz, R., & Müller, U. 2001, *Phys. Fluids*, 13, 561
- Tobias, S. M., Cattaneo, F., & Boldyrev, S. 2013, in *Ten Chapters in Turbulence* (Cambridge University Press)
- Vainshtein, S. I., & Cattaneo, F. 1992, *ApJ*, 393, 165
- Vainshtein, S. I., & Zeldovich, Y. B. 1972, *Sov. Phys. Usp.*, 15, 159
- Verma, M. K. 2004, *Phys. Rep.*, 401, 229
- Waleffe, F. 1992, *Phys. Fluids A*, 4, 350
- . 1993, *Phys. Fluids A*, 5, 677
- Xia, H., Byrne, D., Falkovich, G., & Shats, M. 2011, *Nature Physics*, 7, 321